FURTHER INSIGHTS INTO THE STRUCTURE OF 30 DORADUS FROM THE *HUBBLE SPACE TELESCOPE* INSTRUMENTS[1]

NOLAN R. WALBORN AND JESÚS MAÍZ-APELLÁNIZ

Space Telescope Science Institute, 3700 San Martin Drive, Baltimore, MD 21218; walborn@stsci.edu, jmaiz@stsci.edu

AND

RODOLFO H. BARBÁ[2]

Facultad de Ciencias Astronómicas y Geofísicas, Universidad Nacional de La Plata, Paseo del Bosque,
1900 La Plata, Argentina; rbarba@fcaglp.fcaglp.unlp.edu.ar

ABSTRACT

New observations with the *Hubble Space Telescope* Wide Field Planetary Camera 2 (WFPC2), combined with prior archival data, provide nearly complete coverage of the inner 30 Doradus Nebula in both nebular lines and continuum at $0\rlap{.}''1$ resolution. The developing windblown cavity surrounding the massive first-generation, central cluster and its interface with the remanent molecular clouds, the site of second-generation, triggered star formation, are imaged in their entirety. Dithered Planetary Camera observations with $0\rlap{.}''03$ resolution of Knots 1–3 reveal further structural details of the large dust pillars oriented toward the central cluster and the newborn, massive multiple systems of the second generation in those fields. The new data also provide the first WFPC2 coverage of the fields of two interesting, luminous infrared sources observed in our previous Near Infrared Camera and Multi-Object Spectrometer program; comparisons of the high-resolution optical and IR images are illuminating. In addition, we have obtained Space Telescope Imaging Spectrograph optical, long-slit observations of seven O-type multiple systems in the region, including those in Knots 1–3 and four representatives of the older generation. The spatially resolved spectrograms and classifications of the close pairs, with separations ranging from $0\rlap{.}''09$ to $1\rlap{.}''18$, are presented, as well as WFPC2 photometry of the individual components and the compact clusters of fainter stars associated with them. These new observations, and planned further analysis of them, offer significant new information about the intricate structure and evolution of the two-stage starburst in 30 Dor.

Key words: galaxies: starburst — H II regions — ISM: individual (30 Doradus) — Magellanic Clouds — stars: early-type — stars: formation

1. INTRODUCTION

The praises of 30 Doradus are often sung and need not be echoed here; suffice it to recall that it is the largest H II region in the Local Group, and the most propitious representative of its age group for investigation of the spatial and temporal characteristics of a starburst in fine detail. In recent years, the *Hubble Space Telescope* (*HST*) has contributed qualitative advances in our knowledge of 30 Dor, because of its high spatial resolution and ultraviolet sensitivity. Photometry in images from the *HST* cameras of thousands of individual stars in the massive central cluster, including its dense core R136, has revealed a normal initial mass function and a total mass of $\sim 2 \times 10^4~M_\odot$ (Hunter et al. 1995a, 1996, 1997; Parker, Heap, & Malumuth 1995; Sirianni et al. 2000). Spatially resolved spectroscopy of dozens of the brighter members of the inner cluster with the *HST* spectrographs has found the richest concentration of the most massive hot stars (spectral types O2–O3) that is accessible to such observations (de Koter, Heap, & Hubeny 1997, 1998; Massey & Hunter 1998; Walborn et al. 2002). *HST* nebular

imaging has shown intricate structural details, providing the essential insight that the brightest nebulosity comprises the narrow interface between the central cavity being evacuated by the stellar winds, and the surrounding molecular clouds (Hunter et al. 1995b; Scowen et al. 1998; Rubio et al. 1998). Infrared images from *HST* have discovered surprising characteristics of the new stellar generation being triggered at and near that interface (Walborn et al. 1999a; Brandner et al. 2001).

In this paper, we present further observations of 30 Dor with the *HST* Wide Field Planetary Camera 2 (WFPC2) and the Space Telescope Imaging Spectrograph (STIS), which offer useful additional information about this unique region. The new WFPC2 images essentially complete the partial coverage of the inner nebula available from previous programs and provide higher spatial resolution for three subfields of special interest. They also include the fields of two luminous IR sources observed in our earlier *HST* Near Infrared Camera and Multi-Object Spectrometer (NICMOS) program, which are compared with the new optical images here. The STIS long-slit spectroscopy resolves several O-type multiple systems outside the cluster core, including representatives of both the younger second stellar generation and the older first generation. WFPC2 photometry of these objects is also presented, based on archival and new images. Finally, further measurements and analyses of these data planned for future papers are previewed.

[2] Member of the Carrera del Investigador Científico, CONICET, Argentina.

2. OBSERVATIONS

2.1. *WFPC2*

Previously, only partial *HST* WFPC2 coverage of 30 Dor was available, comprising the three, asymmetrically located WFC fields when the clusters R136 (programs 5114, principal investigator J. Westphal, and 5589, PI J. Trauger) and Hodge 301 (program 6122, PI Y.-H. Chu) were centered in the Planetary Camera (PC) chip. Furthermore, program 5114 contains only continuum filter exposures. We have remedied this situation in our program 8163, with two WFPC2 continuum pointings designed to cover the gaps, and three nebular-line pointings with Knots 1–3 centered in the PC and field rotations again planned to complete coverage of the inner nebula insofar as possible. (The southern continuum field observed the association surrounding the luminous blue variable R143 [Parker et al. 1993; Walborn & Blades 1997] and is not discussed in this paper.)

The continuum observations were done in 1999 October and the nebular-line observations in 2000 March, April, and September. Table 1 lists details of the WFPC2 data. Successive columns identify the fields, the pointing coordinates for equinox J2000, the dates of the observations, the filters, and the exposure times. Each continuum observation consisted of a short and a long exposure, the latter split in half for cosmic-ray removal, in order to cover the stellar magnitude range of interest (12–21) without saturation. The nebular-line observations were dithered to increase the resolution, in a four-point box pattern for F673N and a dual pattern for the other filters.

2.2. *NICMOS*

The NICMOS images in 30 Dor were obtained under *HST* program 7819 during 1998 February and March. The data have been described in Walborn et al. (1999a) and Brandner et al. (2001), so only a few details pertinent to those shown here will be repeated. They were obtained with NICMOS camera 2, which has a $19''$ square field of view, through broadband filters F110W (approximately *J*),

F160W (*H*), and F205W (*K*), with total exposure times of 320, 384, and 448 s, respectively, split equally between two dithered positions. The present images have been processed through the STScI data pipeline, including subtraction of the thermal background at *K* by means of a blank-field observation, and they have not been deconvolved.

2.3. *STIS*

During prior work with the WFPC2 and NICMOS images, a number of interesting close visual binaries or multiple systems were noted among the 30 Dor stellar populations outside of R136, including the systems in all of Knots 1–3. In order to understand the content of these systems, spatially resolved spectroscopy is required. Such was included in our *HST* program 8163, by means of the long-slit capability of STIS. The optimum wavelength region for spectral classification and subsequent quantitative analysis of OB stars is the blue-violet, 3900–4800 Å. Neither of the two STIS/CCD configurations covering this region is ideal for these purposes: although the spectral coverage of the lower resolution G430L configuration (2900–5700 Å) is more than ample, its 2 pixel resolution of 5.5 Å is rather lower than desirable, while the higher resolution G430M configuration offers more resolution (0.56 Å) than necessary at least for classification but covers only 286 Å per observation, which together with the supported central wavelengths requires four exposures to provide the desired wavelength coverage (settings at 3936, 4194, 4451, and 4706 Å). This situation has been recounted at some length to explain the observing strategy adopted: for the brighter systems, the optimum four G430M observations were obtained; for the systems of intermediate brightness, the three longest wavelength G430M settings were obtained; and for the faintest systems, only the single G430M setting covering the crucial lines He I $\lambda\lambda4387$, 4471 and He II $\lambda4541$, as well as Hγ, was observed, supplemented by a G430L observation. In all cases, the STIS long slit was oriented at the position angle of the separation between the brightest binary components in the systems.

TABLE 1
WFPC2 Observations

Field	R.A. (J2000)	Decl. (J2000)	Date	Filter	Exp. Times (s)
Knot 1..............	55 38 52	−69 05 18	2000 Sep 21	F502N	2 × 500
				F656N	2 × 400
				F673N	4 × 500
Knot 2..............	5 38 43	−69 04 24	2000 Apr 21	F502N	2 × 500
				F656N	2 × 400
				F673N	4 × 500
Knot 3..............	5 38 28	−69 05 57	2000 Mar 29	F502N	2 × 500
				F656N	2 × 400
				F673N	4 × 500
North..............	5 38 39	−69 04 39	1999 Oct 5	F336W	10 + 80
				F555W	3 + 80
				F814W	5 + 80
South	5 38 50	−69 07 50	1999 Oct 4	F336W	10 + 80
				F555W	3 + 80
				F814W	5 + 80

NOTE.—Units of right ascension are hours, minutes, and seconds, and units of declination are degrees, arcminutes, and arcseconds.

TABLE 2
STIS OBSERVATIONS

Star	R.A. (J2000)	Decl. (J2000)	Sep. (arcsec)	P.A. (deg)	Date	Wavelength[a] (Å)	Exp. Time (s)	S/N
P409AB	5 38 34	−69 06 04	0.16	60	1999 Oct 20	4300	2588	112/100
P1222/P1201	5 38 45	−69 05 09	1.18	309	2000 May 23	4451	3088	40/36
						4194	650	39/30
						4451	650	39/30
P1429AB.............	5 38 48	−69 04 43	0.30	286	2000 May 21	4706	740	40/30
						4300	1070	110/39
P304/P294	5 38 33	−69 04 32	0.65	301	2000 May 25	4451	1224	37/15
						3936	428	48/38
						4194	432	48/39
						4451	432	47/38
P1231AB.............	5 38 45	−69 05 47	0.09	55	1999 Oct 13	4706	480	47/37
						3936	430	46/45
						4194	430	46/45
						4451	430	45/44
P1306/P1304	5 38 46	−69 05 55	0.47	189	2000 Feb 2	4706	482	46/45
						4194	650	40/38
						4451	650	39/38
P1312AB.............	5 38 46	−69 05 52	0.12	64	1999 Oct 13	4706	740	40/39
						3936	420	37/37
						4194	420	37/37
						4451	410	35/35
						4706	520	38/38

[a] The central wavelength of G430L is 4300 Å; other central wavelengths are G430M settings.

The STIS observations were performed from 1999 October through 2000 May. Table 2 lists characteristics of the stellar systems and the observations, first for the three young systems in Knots 1–3, followed by four older systems. Successive columns give the stellar identification from Parker (1993), coordinates for equinox J2000, the separation of the binary components, the position angle of the fainter component from the brighter, the date of the observations, the STIS grating settings observed, the exposure times, and the peak signal-to-noise ratio per 2 pixel resolution element in each spectrogram.

For completeness, we mention that an eighth object, Parker 644, was also observed with the single G430M setting and G430L. This interesting faint star is located near the southern end of the western interface and appears to be very young, similarly to Knots 1–3. It is an IR source (Rubio et al. 1998 IRSW-98; NICMOS field 1 is reproduced in Brandner et al. 2001) and has associated nebular knots, one of which is resolved in the STIS spectrograms. Unfortunately, the higher resolution STIS observation is too noisy to be useful, and at the lower resolution the stellar spectrum is nearly featureless, with only some high Balmer series members detected in absorption. We are uncertain whether the latter results are primarily physical or observational; in any event, these data are not discussed further here.

3. REDUCTIONS

3.1. WFPC2 Images

The WFPC2 images were reduced with two different procedures. The four continuum and five narrowband pointings were jointly processed to produce $272'' \times 179''$ mosaics at $0\rlap{.}''10$ resolution, while the three new narrowband dithered PC fields were used to produce $33'' \times 33''$ images at an enhanced $0\rlap{.}''032$ resolution. The reductions were carried out with both standard STSDAS/IRAF[3] packages and custom-made IDL routines.

The first step was to update the WFPC2 group parameters affected by plate-scale, shift, and rotation changes due to project database updates with the WFPC2 task uchcoord (Biretta et al. 2000). A correction was found to be necessary for the data from programs 5114 and 5589. The second step was to eliminate cosmic rays. For the three new narrowband dithered pointings, this step was done with a combination of the DITHER package (Koekemoer et al. 2000) and the WFPC2 task crrej. For the rest of the data we simply used crrej.

At this point, we were able to produce the final narrowband, high-resolution PC images of the three knots by using the standard DITHER procedures. Color images were produced from these data in two ways: with F502N and F656N in the green and red channels, respectively, and with F502N and F673N in the green and red channels, respectively (note that the blue channel is not used for these images).

On the other hand, the production of the large lower resolution mosaics was somewhat more complicated. We first corrected for geometric distortions using the WFPC2 task wmosaic and photometrically calibrated each field. The next step was to combine all the continuum and narrowband pointings into a single $272'' \times 179''$ mosaic. In order to do that, one has to take into account that the precision of the absolute astrometry in the WFPC2 headers is determined by that of the Guide Star Catalog, which is typically $1''$ (10

WFC pixels). This effect is quite large when one combines different WFPC2 pointings, and it has to be corrected. To do so, we applied the crossdriz task in the DITHER package in selected regions common to pairs of different pointings and then corrected for the relative displacements, which were indeed found to be of the order of $1''$. Finally, we used a procedure similar to that outlined in MacKenty et al. (2000) to eliminate the nebular contribution to the continuum filters and produce "pure continuum" images. We also tried the same procedure to eliminate the continuum contribution to the narrowband filters, but we decided not to use it because of the introduction of artifacts due to the existence of uncorrected geometric displacements and distortions at the $0''.1$ (1 WFC pixel) level (these distortions are unimportant in the continuum mosaics because of the point-source nature of the stellar images). The above procedure was applied to the data to produce three continuum (WFPC2 U, V, and I) and three narrowband (F502N, F656N, and F673N) multiple-pointing mosaics. Along the way we applied several procedures to eliminate cosmetic defects such as bad pixels, low-signal interchip regions, and saturated stars. We also eliminated by hand the noisy pixels in the short-exposure F336W images from program 5114. In order to produce an RGB color mosaic of the full field that represented gas excitation and intensity, as well as star colors and brightnesses, we first discarded the F502N mosaic, since F673N and F656N contain the required information. Our idea was to show stars in "near-true" color by using WFPC2 I, V, and U for the red, green, and blue channels, respectively, and to include the information about the gas by adding F673N and F656N to the red and green channels, respectively. When we tried to do that, we found that the contrast between the bright and dim regions in F673N was so large that it was not possible to show the structures present at different intensity levels. To reduce the contrast, we subtracted from the original mosaic a 101×101 pixel median-filtered version of itself multiplied by a positive coefficient smaller than 1. We also discovered that the continuum contamination in the F673N and F656N filters changed the color of all stars into red or orange. This problem was solved by masking the positions of the stars in those filters. With those corrections implemented, the final result displayed below was obtained.

3.2. *STIS*

The standard procedure for extracting STIS CCD spectrograms is to obtain a wavelength calibration [which produces a $\lambda(x)$ function, where x is the horizontal pixel coordinate] and to sum over a range of pixels in the spatial direction of the detector (y) in order to produce the flux at a given λ after the background is subtracted. Such a procedure would not work for most of our observations, because of the overlapping spatial profiles produced by the small separations between pairs of stars. Therefore, we fitted the data at each x-position with a double-peaked spatial profile in order to produce the flux as a function of λ for each of the two stars. We tested different alternatives for the double-peaked function (Gaussians, Gaussians with additional wings, and Gaussians integrated over the spatial direction for each pixel), but the results were nearly independent of the choice made. The discussion below refers to the third profile (spatially integrated Gaussians), but its modification for the other two cases is straightforward.

Our goal is to obtain three parameters for each of the two stars at each x-coordinate: $I_0(x)$ (the peak intensity), $y_0(x)$ (the spatial position of the peak), and $\sigma(x)$ (the width of the fitting profile). The parameter $y_0(x)$ is not a constant, since there is a displacement of a few pixels between $x = 1$ and $x = 1024$ caused by the grating alignment. In principle, one would think that the six parameters at a given x (three for each star) could be allowed to vary in a completely independent way to produce the final result. However, there is a numerical problem that impedes such a procedure. As each profile moves from a pixel center [half-integer values of $y_0(x)$] to a pixel edge [integer values of $y_0(x)$], the discrete nature of the sampled profile shifts flux from one star to the other during the fitting procedure by introducing a nonphysical oscillation as a function of x in the values of $y_0(x)$ and $\sigma(x)$. We solved this problem in three steps. (1) In a first pass, we fitted all three parameters [$I_0(x)$, $y_0(x)$, and $\sigma(x)$] for each of the two stars at each x-position. (2) From those results, we fitted a straight line to each $y_0(x)$ and repeated the fitting procedure, fixing the value of the two $y_0(x)$'s to those obtained from the fit. (3) From the results of the previous step, we now fitted a parabola to each of the $\sigma(x)$. Then, we did a final pass fixing each of the $y_0(x)$ and $\sigma(x)$ [i.e., leaving only the two $I_0(x)$'s as free parameters] in order to obtain the two final values of $I_0(x)$. The integrated fluxes for each star [proportional to $I_0(x)\sigma$] were then rectified to produce the final spectrograms.

3.3. *WFPC2 Photometry*

The photometric results presented here are concentrated in small areas around the spectroscopic targets. These results are extracted from a complete photometric analysis of about 20,000 stars down to $V = 25$ in the WFPC2 images of the 30 Dor Nebula; a more detailed description of the reduction process will be presented in subsequent papers (Barbá et al. 2002).

All broadband WFPC2 images were calibrated with standard STSDAS/IRAF procedures. The photometric analysis was performed with two different software packages, HSTphot (Dolphin 2000a) and IRAF/DAOPHOT (Stetson 1987), to provide internal checks. The results presented here are derived mainly from HSTphot; DAOPHOT was used to recover photometric information for several important stars with special circumstances, such as those located in vignetted regions of the chips.

The HSTphot package (Dolphin 2000a, 2000b) is specifically designed to handle the characteristics of the WFPC2 images by means of a library of Tiny Tim (Krist 1995) undersampled point-spread functions (PSFs); it also contains a set of programs for general reduction procedures such as masking, cleaning, and combining WFPC2 images. Version 1.1 (2001 October) was used here. The first step was to mask all bad and saturated pixels identified in the data-quality images with the procedure mask. The next step was to remove cosmic rays from the images with the procedure crmask. This task can clean images that are not perfectly aligned, and it can handle images with different filters, when the individual observations were not split (as was the case for the F336W image in program 5114). For each of five different WFPC2 pointings and three broadband filters, a combined deep image was produced with the procedure coadd. The final required steps getsky and hotpixels

were applied to the combined images to compute sky background and clean hot pixels. The hstphot routine (named multiphot in version 1.0 of the package) was run on the images from each of the five pointings. This is a powerful task that performs stellar PSF photometry on multiple images in a single run, including alignment and aperture corrections, PSF modification to compensate for geometric distortion (Holtzman et al. 1995) and the 34th-row error (Shaklan, Sharman, & Pravdo 1995; Anderson & King 1999), and correction of charge transfer inefficiency (Dolphin 2000b). During the run of hstphot, the determination of the "local sky" parameter was enabled because of the very nonuniform nebular background in the 30 Dor Nebula. A "sharpness" parameter and a measure of the quality of the fit (χ^2) were used to reject false star detections in regions with very structured nebulosity or diffraction spikes of bright stars, among other artifacts. Additional star rejections were made by visual inspection of the images.

The photometric results presented in Tables 4–8 correspond to stars contained in a $12'' \times 12''$ box around each spectroscopic target, with F555W magnitudes brighter than 20.5. The magnitudes are in the WFPC2 flight system as defined by Holtzman et al. (1995), but with new photometric zero-point calibrations derived by Dolphin (2000b). The X- and Y-coordinates are in the chip coordinate systems of the F555W images, with the HSTphot convention (0–799).

Stars P1304 and P1306 were observed in images from program 5114, and they are in the vignetted region of chip 2 ($Y < 46$); therefore, some loss of light is expected. We estimate the loss for those stars to be about 30% from linear interpolation between values of 50% illumination at $Y = 26$ and full illumination at $Y = 46$ (see Table 2.5 of Biretta et al. 2000). The magnitudes for stars in the vignetted region were obtained with IRAF/DAOPHOT, since HSTphot is disabled in that region. However, no accurate correction of the vignetting itself is available, and further aspects of the IRAF/DAOPHOT application there will be discussed in subsequent papers.

4. RESULTS AND DISCUSSION

4.1. *Structure of the Inner 30 Dor Nebula*

Figure 1 is a nearly complete mosaic of the inner 30 Dor Nebula, based on seven WFPC2 pointings, four from the current program and three from the archives, as detailed in the preceding sections. The color coding of the filters is as follows: blue is WFPC2 U, green is H$\alpha + V$, and red is [S II] $+ I$. Thus, the hot stars are blue, while high-excitation gas exposed directly to the hot stars is green, low-excitation gas shielded from direct sight lines to the hot stars is red, and the interfaces between the high-excitation cavity and surrounding molecular clouds show as yellow. The dense core of the ionizing cluster, R136, is below center. The older cluster with red supergiants at upper right is Hodge 301, analyzed in these images, from their *HST* program, by Grebel & Chu (2000). Figure 1 serves double duty as a chart locating seven subfields to be discussed in subsequent sections: the PC fields of Knots 1–3, NICMOS fields 15 and 16, and two smaller fields containing the older O-type multiple systems measured spectroscopically and photometrically.

It is now well established that 30 Dor is (at least) a two-stage starburst: the central cluster has an age of about 2 Myr, while there is a younger, evidently triggered second stellar generation less than 1 Myr old developing along the surrounding cavity interface (Walborn & Parker 1992; Rubio, Roth, & García 1992; Hyland et al. 1992; Parker & Garmany 1993; Walborn & Blades 1997; Rubio et al. 1998; Walborn et al. 1999a; Brandner et al. 2001). Attributes of the new generation include massive young stellar systems in dense nebular knots, dust pillars oriented toward the central cluster, IR sources often within or near the pillars, and jets associated with several IR sources. Some of these features are visible in Figure 1, and several will be shown at a larger scale below. The remanent molecular material is concentrated to the northeast and southwest of the central cluster (Werner et al. 1978; Rubio et al. 1998; Johansson et al. 1998), beyond the bright interfaces in those directions.

Figure 1 reveals the full extent of the 30 Dor interface. Its projected distance from the cluster core ranges from about 10 to 20 pc. It is more extended to the north, following the diffuse extension of the ionizing cluster in that direction. On the other hand, the east-west asymmetry may be due to a lower ambient density in the former direction. It is noteworthy that the interface and molecular material lie predominantly in one hemisphere relative to the cluster core. That morphology is ubiquitous among starbursts on this scale (Walborn 2002), suggesting that the initial burst was triggered near the surface of the original giant molecular cloud by an external event, rather than by a collapse of the cloud toward its center. The next evolutionary phase of 30 Dor will be a giant shell H II region, with an evolved central association in a completely evacuated cavity, and with the nebulosity and early O stars around the periphery, as in Henize N11, the second-ranked H II region of the Large Magellanic Cloud (Parker et al. 1992; Walborn & Parker 1992; Walborn et al. 1999b; Heydari-Malayeri et al. 2000). The projected radius of the N11 cavity is 30–40 pc; its central association is 3.5 Myr old and has produced many supernovae, whereas there may not have been any yet in the core of 30 Dor, because the most massive stars are still there. The energetics of N11 has been modeled by Meaburn et al. (1989) and Rosado et al. (1996). Thus, the 30 Dor cavity and second stellar generation are still under construction, being primarily products of the stellar winds from the central cluster; ultimately they will become substantially more extensive than at present, once the imminent supernovae have added their contribution.

In further analysis underway with M. Rubio, the structural information from Figure 1 will be combined with new H$_2$ and CO data, including velocity information, to develop an improved three-dimensional physical model of 30 Dor.

4.2. *Fields of Knots 1–3*

The objects called Knots 1–2 were identified as very young O stars within dense nebular condensations in the filaments northeast of R136 by Walborn & Blades (1987); Knot 3 in the filament west of R136 was added by Walborn (1991). It was suggested then that these objects represented ongoing star formation in 30 Dor. Of course, it is these "filaments" in ground-based images that have been revealed by WFPC2 as the interfaces between the central cavity and surrounding molecular clouds. Figures 2–4 display the dithered PC images with 0″03 resolution of Knots 1–3, respectively. In each of these figures, the left panel shows [O III] in
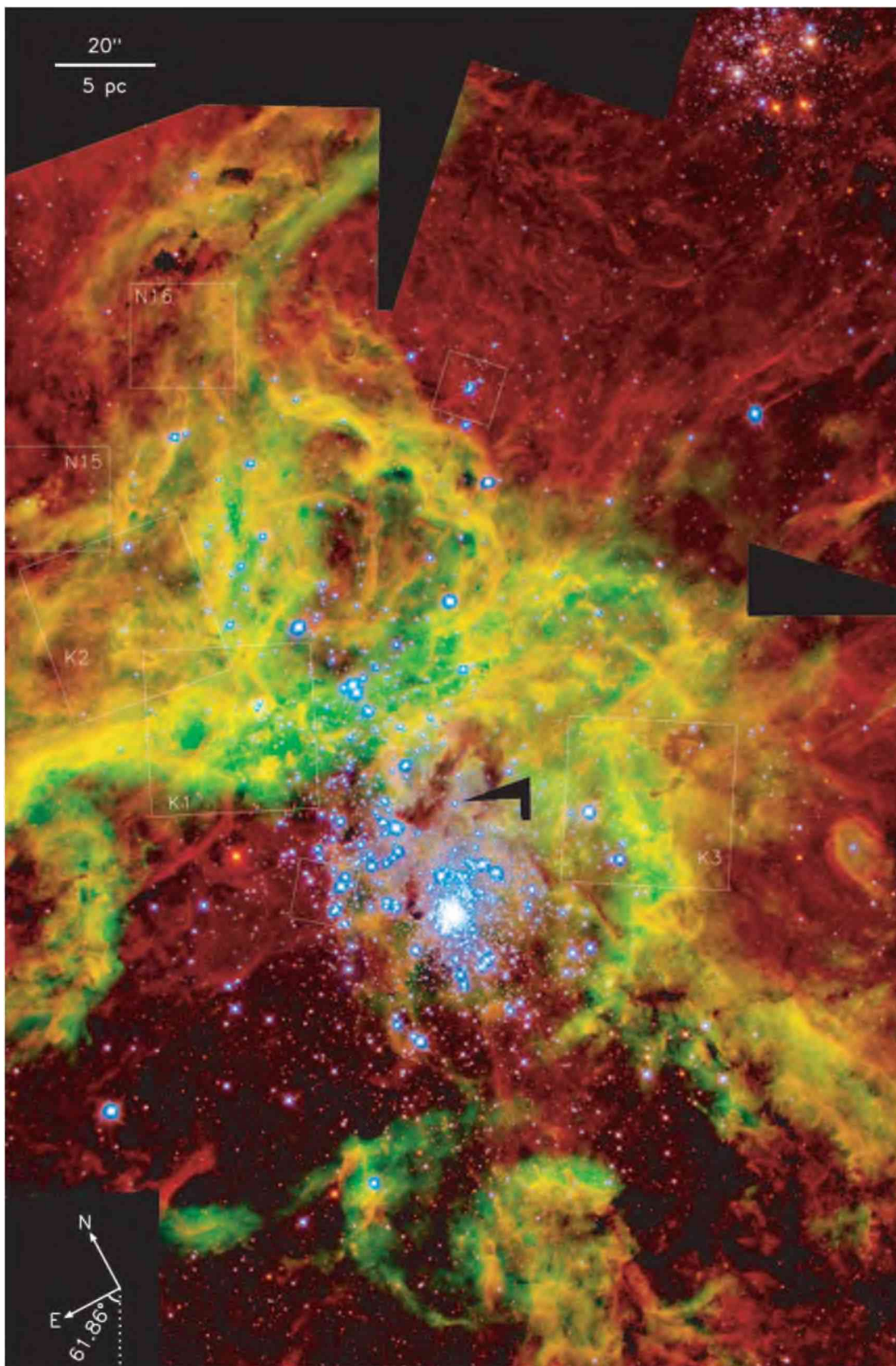
Fig. 1.—Mosaic of WFPC2 images of 30 Dor. Blue is WFPC2 U, green is Hα + V, and red is [S II] + I. The bright yellow features are the interfaces between the central cavity and surrounding molecular clouds. Pure black spaces lack nebular-line or continuum coverage, or both. The large white boxes labeled K1–K3 are the 33″ square PC fields of Knots 1–3. The intermediate boxes labeled N15 and N16 are 19″ square NICMOS fields. The two small boxes are 12″ square and contain multiple stellar systems studied here; the P294/P304 system is to the north, while the southern field contains P1231, P1304/P1306, and P1312.
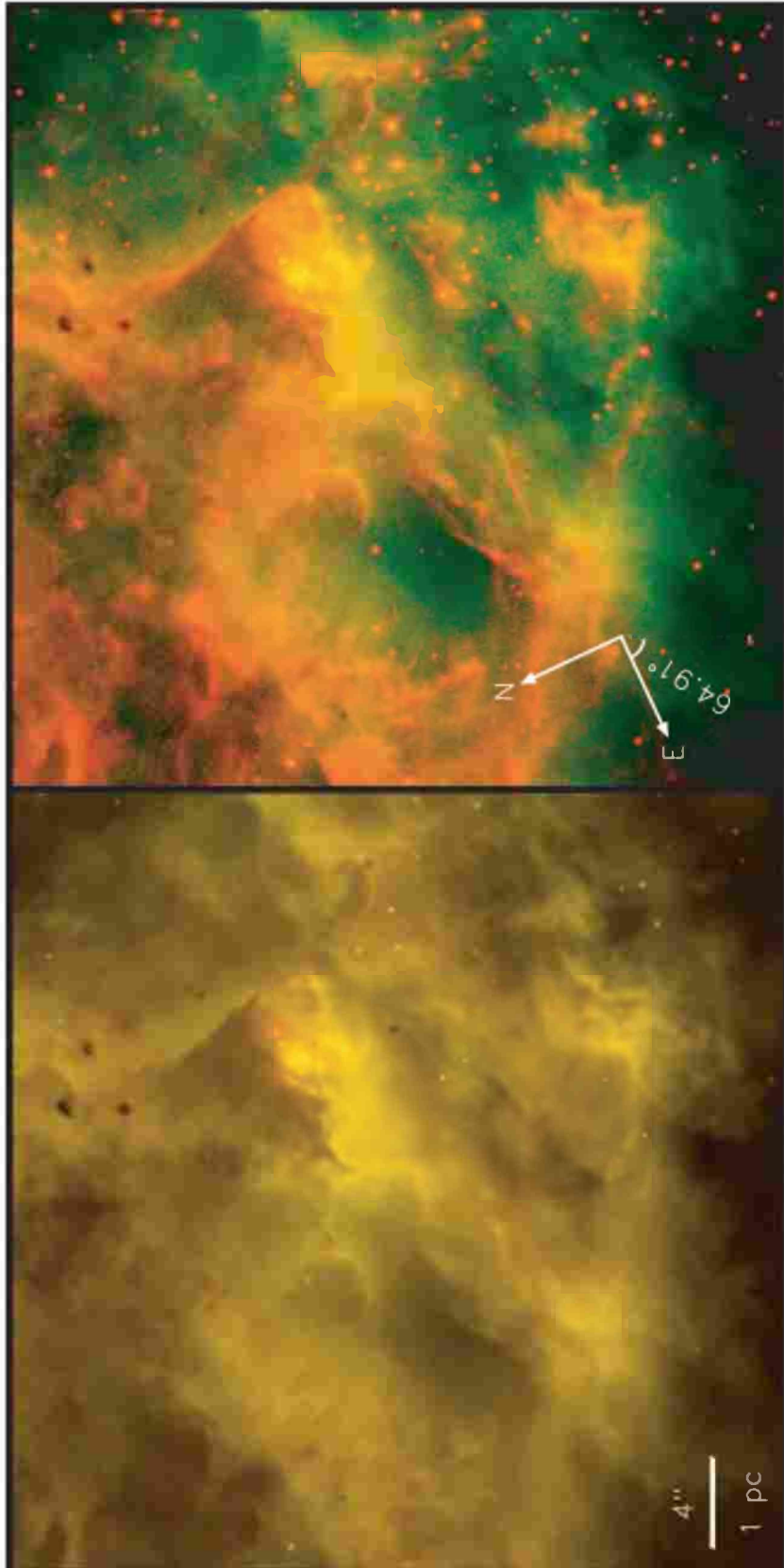
FIG. 2.— Dithered PC images of Knot 1. In the left panel, green is [O III] and red is Hα, while at the right green is [O III] and red is [S II]. See the text for discussion.
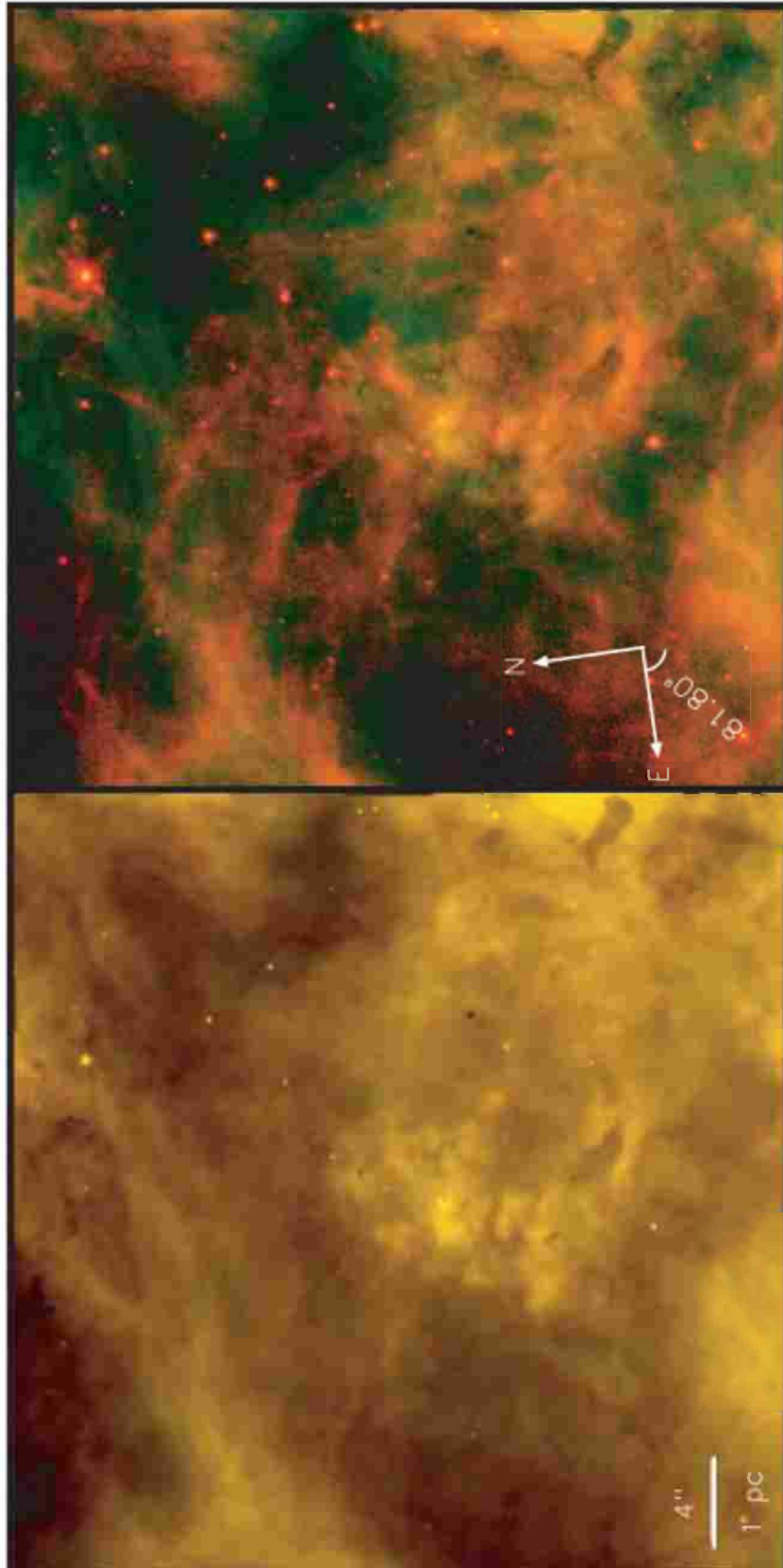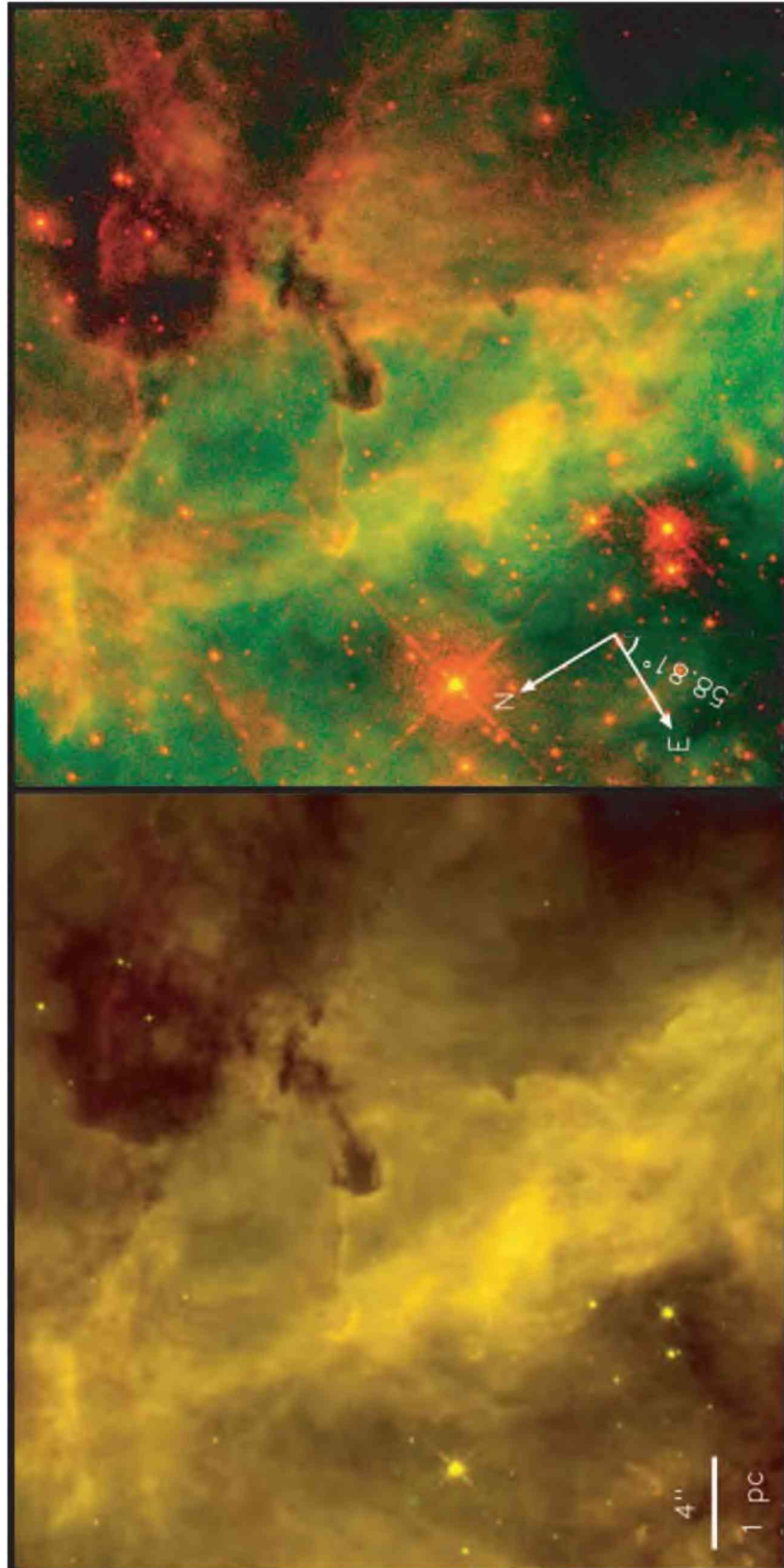
FIG. 3. — Same as Fig. 2, but for Knot 2

Fig. 4.—Same as Fig. 2, but for Knot 3

green and Hα in red, while the right panel is [O III] green plus [S II] red; the two filter combinations reveal rather different aspects of the nebular structures in these regions. NICMOS *JHK* composite images of these fields were compared with lower resolution WFPC2 data in Walborn et al. (1999a); at that time, only continuum images of Knots 1–2 were available from WFPC2.

The new images of Knot 1 (Fig. 2) provide higher definition of the nebular structures and the newborn, massive Trapezium system that includes Parker (1993) stars P1201 and P1222 (which are identified and further discussed in § 4.4.1 below). As discussed in Walborn et al. (1999a), the stellar system has just blown off the summit of its natal pillar, oriented toward R136, creating a celestial facsimile of Mount St. Helens. The [O III] + Hα representation shows clearly that the third component of the system is redder than the others and appears to have a red nebular halo, indicating that it is still more deeply embedded in the dust cloud than its two brighter companions. The [O III] + [S II] frame shows well which nebular structures in the region have lower and/or collisional ionization. Walborn et al. (1999a) also shows a rich cluster of faint IR stars associated with the Knot 1 Trapezium; two very luminous IR sources embedded in the adjacent, intact pillar to the east of Knot 1; and a faint, very red IR source within the easternmost of the three dark globules north of Knot 1. Rubio et al. (1998) and Johansson et al. (1998) chart massive molecular concentrations just north of these pillars, opposite to the direction of R136; that is, these structures and the new stars they contain have likely been formed on the side of the cloud facing R136 by the energetic stellar outflows from the latter.

The images of Knot 2 in Figure 3 again reveal further intricacy of the nebular structures. The brightest optical star in the knot is P1429A, just below and left of center in the frames; it turns out to be of very early spectral type (§ 4.4.1 below). A primary motivation for these observations was to search for optical structures related to a stellar jet in Knot 2, inferred from two extended IR sources oppositely aligned across the stellar system (Walborn et al. 1999a). However, no features associated with the nonstellar sources or the presumed linear jet appear in these images. This field contains an H_2O maser for which an accurate position has recently been determined (Lazendic et al. 2002); it does not coincide exactly with any of the IR sources but is nearest to a faint optical star (cf. Rubio et al. 1998).

Figure 4 displays the new PC images of the field of Knot 3, which contains a remarkable array of stellar and nebular structures related to current star formation; they were discussed in some detail in Walborn et al. (1999a) but are seen with improved clarity here. Knot 3 is the bright nebular patch below center, within which the two optical components of P409 (§ 4.4.1 below) can be seen. The two pillars above it, oriented in the general direction of R136, are of outstanding interest. The bright-rimmed one contains a faint optical star within its head, which is one of the brightest stellar IR sources in 30 Dor. The adjacent dark pillar is highly reminiscent of the Orion Horsehead Nebula at this resolution. The characteristics of the 30 Dor pillars and others are intercompared in Walborn (2002) (see also Scowen et al. 1998). The other major molecular concentration in 30 Dor lies beyond these objects with respect to R136 (Rubio et al. 1998; Johansson et al. 1998), so the basic physical structure of this region is entirely analogous to that of Knot 1.

4.3. *NICMOS Fields 15–16*

Hyland et al. (1992) discovered four luminous protostars (P1–P4) in 30 Dor, which not surprisingly turn out to be the brightest of the numerous stellar IR sources found there with subsequent instrumentation. Their P1 is located in the pillar adjacent to Knot 1 and was resolved into two bright sources by Rubio et al. (1998; IRSN-122/126), Walborn et al. (1999a), and Brandner et al. (2001). P3 (IRSW-30 in the subsequent references) is the source in the head of the bright-rimmed pillar just north of Knot 3. P2 (not observed by Rubio et al. 1998) and P4 (IRSN-134/137) were also observed in our NICMOS program and have been measured by Brandner et al. (2001; the NICMOS field numbers are defined in that paper), but they are located further north of R136 than the other sources (Fig. 1) and were not covered by the previous WFPC2 data. Our new WFPC2 fields do include them, so they are compared with the NICMOS images here in Figures 5 and 6, in each of which the left panel displays WFPC2 F336W, F555W, and F814W (approximately *U*, *V*, and *I*) as blue, green, and red, respectively, and the right panel NICMOS *J*, *H*, and *K* analogously.

The images of P4 in field 15, displayed in Figure 5, show that it is a small, heavily embedded cluster, the brighter members of which can be seen in the optical image. We have measured an F555W magnitude of 21.12 and an F814W of 19.60 for the brightest star in the cluster, centered in the NICMOS image. Brandner et al. (2001) measured NICMOS *J* of 17.06, *H* of 15.24, and *K* of 13.48 for this star, in good agreement with the ground-based values of Rubio et al. (1998) for IRSN-137. It will be of some interest to measure and analyze the entire cluster in these images.

In striking contrast, P2 in field 16 (Fig. 6) is completely unresolved in the *HST* images. It is undetected in WFPC2 F555W, implying an upper limit of 23–24 mag, but we have measured it at 20.91 in F814W; it is clearly visible as a very red source in the left panel of Figure 6. From the NICMOS images, Brandner et al. (2001) measured *J* of 15.38, *H* of 13.27, and *K* of 11.71 for this star, the latter value similar to those for P3 and the brighter component of P1. It should be recalled that at the distance of the LMC, 0."1 subtends 5000 AU, but at face value the *HST* images of P2 and P4 imply two qualitatively different modes of massive star formation: fragmentation into a cluster and a monolithic object, respectively.

4.4. *O-Type Multiple Systems*

The spatially resolved STIS spectrograms of seven close visual binaries in 30 Dor are displayed in Figures 7 and 8, the former containing the systems in Knots 1–3, and the latter four systems believed to correspond to the somewhat older first stellar generation. The spectral classifications of the components derived from these data, and a photometric analysis of each, are listed in Table 3. Successive columns give the stellar identification from Parker (1993); the spectral type; the WFPC2 F555W magnitude and F336W–F555W and F336W–F814W colors measured here; E_{B-V} derived from F336W–F555W according to the intrinsic colors and relation given by Massey & Hunter (1998);[4] the absolute visual magnitude M_V derived follow-

---

[4] The color excesses derived similarly from F336W–F814W were twice or more as large and were not used.
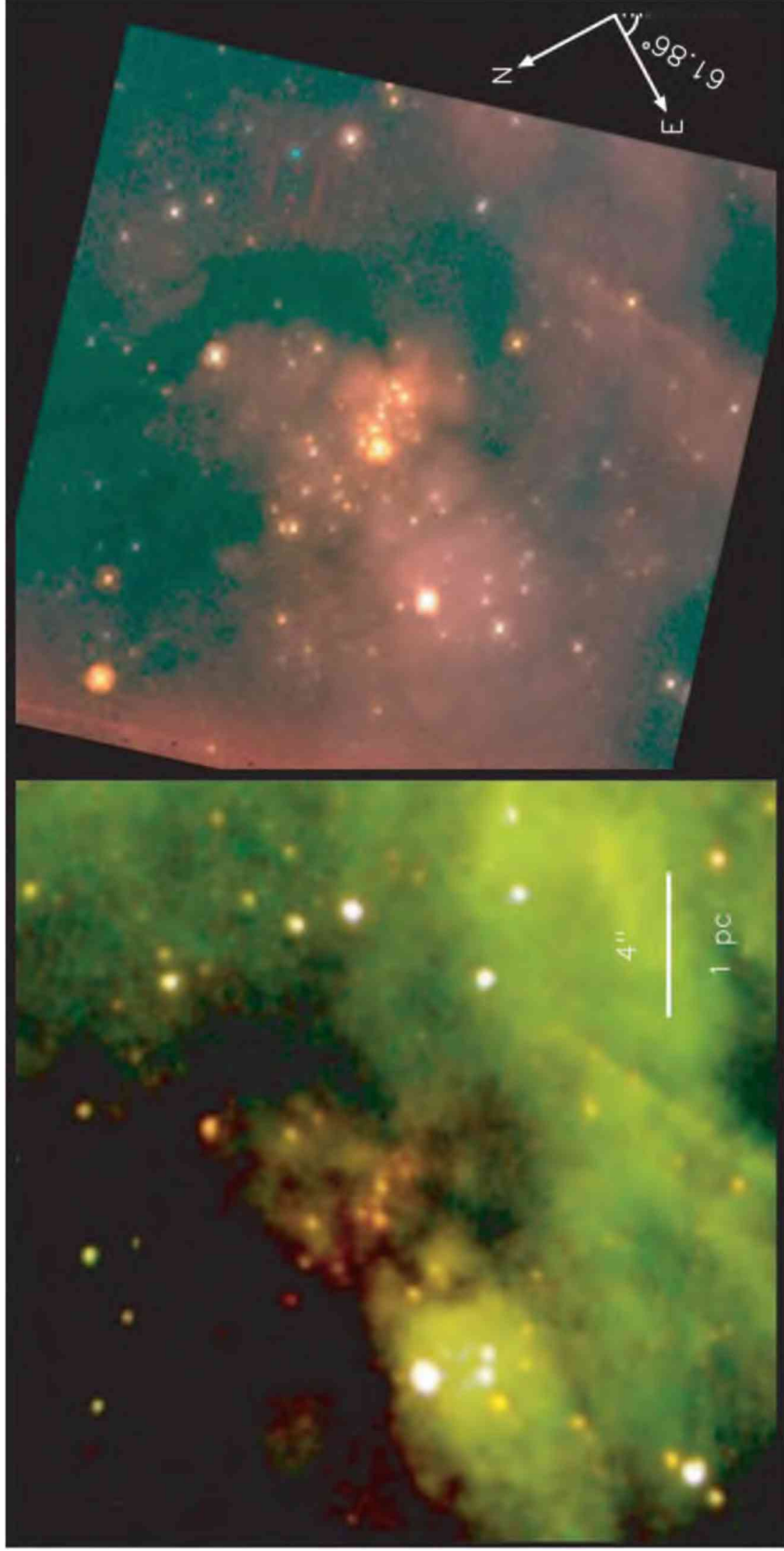
FIG. 5.— Images of the IR cluster P4 in NICMOS field 15. *Left*, WFPC2 *U*, *V*, *I* in blue, green, and red, respectively; *right*, NICMOS *J*, *H*, *K*, analogously. See text for discussion.
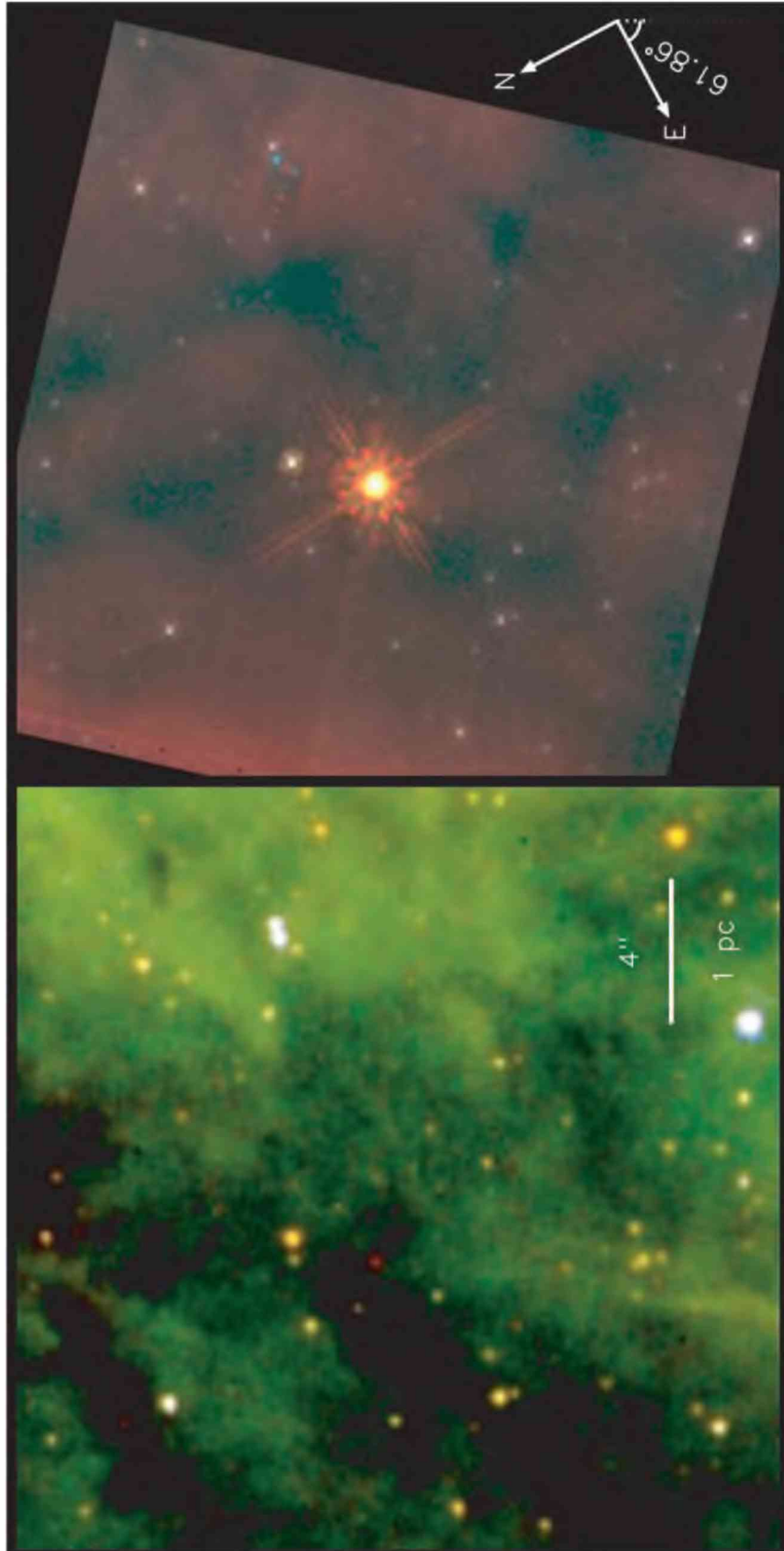
Fig. 6.—Same as Fig. 5, but for the unresolved IR source P2 in NICMOS field 16
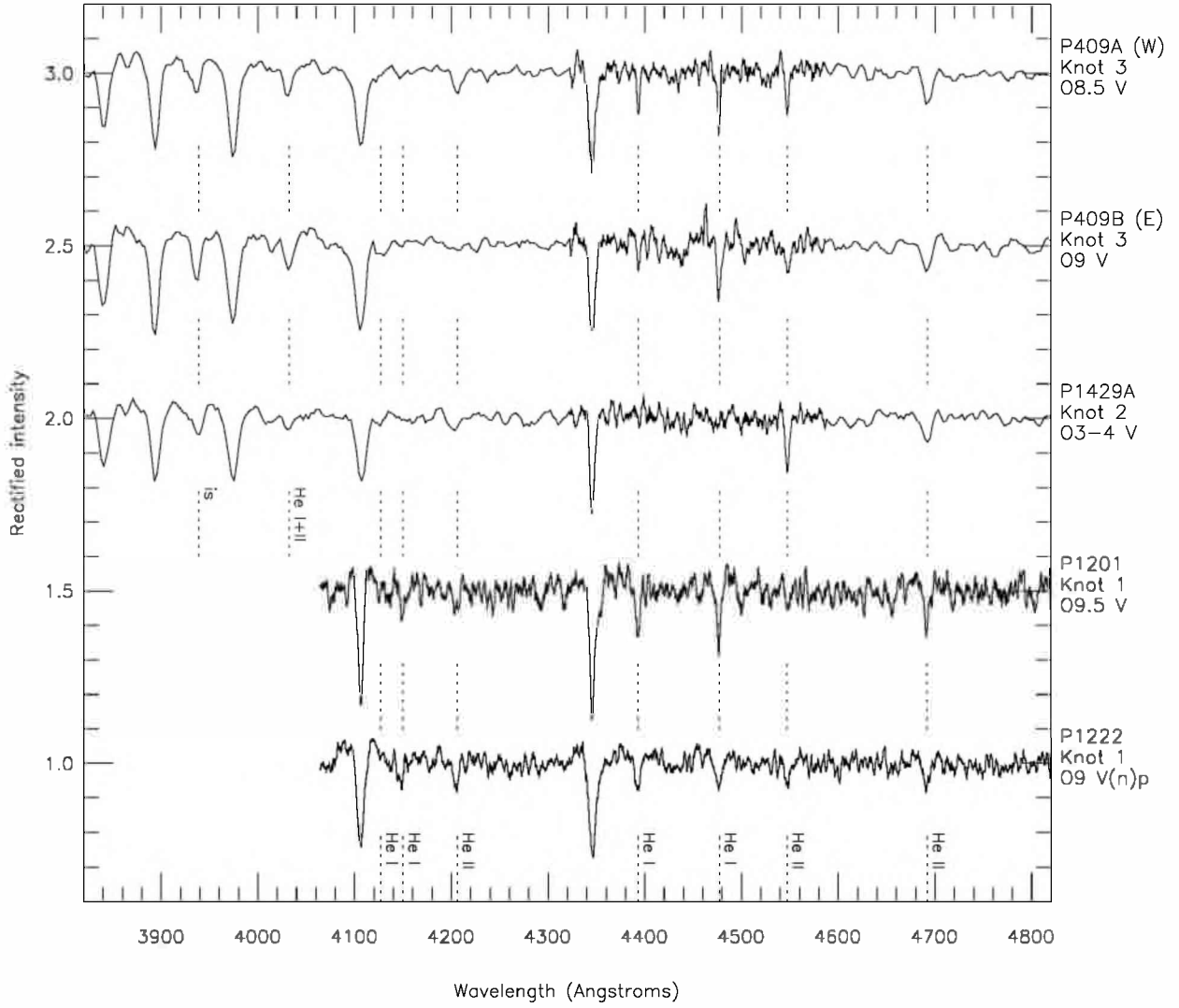
Fig. 7.—Rectified, blue-violet, spatially resolved STIS spectrograms of the brightest components in the Knot 1–3 multiple stellar systems. In the top three spectrograms, the 4310–4590 Å region in the G430L data has been replaced by the G430M observations. The bottom two spectrograms are entirely G430M data. The G430L data have been smoothed by 3 pixels, and the G430M by 11. The absorption lines identified in the spectrum of P1429A are Ca II λ3933 (interstellar) and He I + He II λ4026, while at bottom they are He I λλ4121, 4144, 4387, 4471 and He II λλ4200, 4541, 4686.

TABLE 3
STELLAR PARAMETERS

Star	Spectral Type	m(F555W)	F336W−F555W	F336W−F814W	E_{B-V}	M_V	$M_{V,\text{cal}}$	ΔM_V	M ($M_\odot$)
P409A........	O8.5 V	17.05	−0.70	−0.23	0.54	−3.3	−4.4	+1.1	9
P409B	O9 V	17.08	−0.91	−0.51	0.43	−2.9	−4.3	+1.4	6
P1201	O9.5 V	15.83	−1.28	−0.97	0.25	−3.6	−4.1	+0.5	12
P1222.........	O9 V(n)p	15.11	−1.13	−0.85	0.32	−4.5	−4.3	−0.2	27
P1429A	O3–O4 V	15.88	−1.08	−0.47	0.39	−4.0	−5.5	+1.5	17
P1429B	O8: V:	18.10	−1.14	−0.60	0.32	−1.55	−4.4:	+2.85:	2:
P294...........	O7.5 V	14.90	−1.48	−1.35	0.19	−4.35	−4.8	+0.45	23
P304...........	O9.5 V	14.47	−1.51	−1.47	0.14	−4.6	−4.1	−0.5	30
P1231A	O6 V sb2?	14.55	−1.35	−1.08	0.25	−4.9	−5.3	+0.4	37
P1231B	O7 V	14.61	−1.37	−1.08	0.24	−4.8	−4.8	0.0	35
P1304[a]........	O5 V((f))	15.29	−1.20	−0.88	0.32	−4.4	−5.5	+1.1	24
P1306[a]........	O7 III	15.15	−1.20	−0.80	0.32	−4.5	−5.6	+1.1	16
P1312A	O6.5 V	14.72	−1.20	−0.93	0.32	−4.9	−5.3	+0.4	38
P1312B	O8 V	14.84	−1.12	−0.78	0.33	−4.8	−4.4	−0.4	35

[a] Star located in vignetted region of WFPC2 chip; the listed brightness and mass are underestimates.
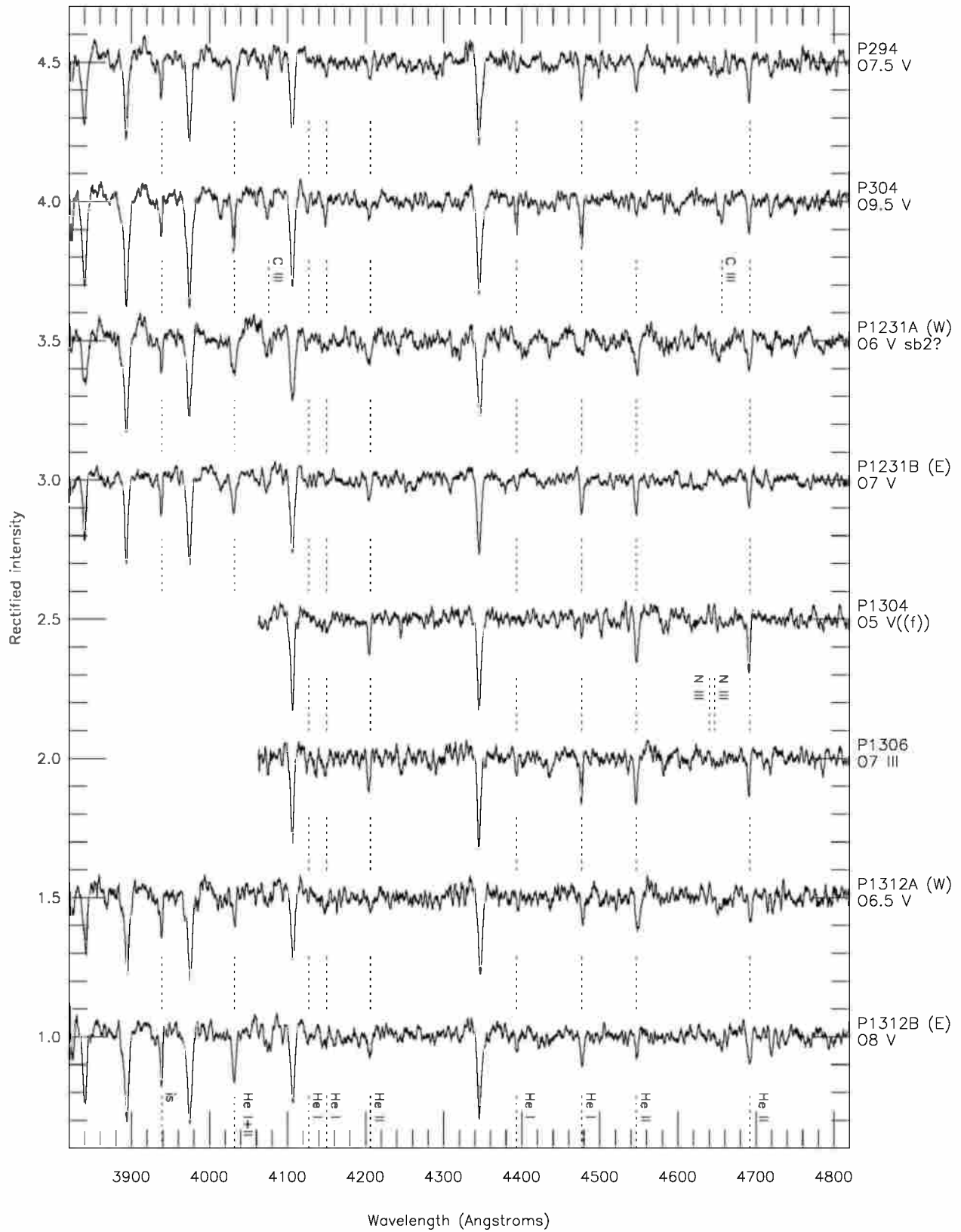
1613

FIG. 8.—Same as Fig. 7, but for the brightest pairs in four older multiple systems. All data are G430M, smoothed by 11 pixels. The absorption lines identified at bottom are as in Fig. 7, with the addition of C III λλ4070, 4650 blends in P304, and N III λλ4634, 4640–4642 emission lines in P1304.

ing Massey & Hunter, but with $V_0 - M_V = 18.6$ and $R_V = 3.0$; the calibration M_V for the spectral type from Walborn (1973); the difference between the two absolute magnitudes, in the sense observed minus calibration; and a stellar mass estimated from the evolutionary calibration of Vacca, Garmany, & Shull (1996), by linear scaling according to the visual luminosity difference at the appropriate spectral type. The results for each system will be discussed below in turn, where WFPC2 charts, a table of WFPC2 photometry for all stars down to F555W magnitude $\sim$20.5 in a 12″ square field containing the multiple system (from which the values in Table 3 are extracted), and color-magnitude diagrams (CMDs) will also be presented for each. (The CMDs contain fainter stars than the tables, which will be listed and fully discussed in Barbá et al. 2002.)

4.4.1. *Knots 1–3*

The spectroscopic and photometric results for these three very young stellar systems are listed in the first part of Table 3, where it can be seen that most of the components are subluminous relative to the calibration, consistent with extreme youth. On the other hand, it is also possible that an abnormally high value of R_V applies in these regions, in which case the derived M_V's would become brighter. This possibility will be investigated in future analyses combining the optical and IR (Brandner et al. 2001) photometry. The very small masses derived for some of these stars (Table 3) are probably unrealistic, indicating either that the linear scaling by visual luminosity is inappropriate over such large ranges, or that in fact R_V is larger than 3.0. (In addition, the spectral type of P1429B is uncertain, as further noted below.)

Charts for the field of P409 in Knot 3 are given in Figure 9 (see also Fig. 4), the photometry in Table 4, and the CMDs in Figure 10. The two classified optical components

are of similar late O types, although the combined light had been given an early O classification from ground-based data by Walborn & Blades (1997); the nebular emission-line contamination is of course strongly suppressed by the *HST* spatial resolution. P409C (star 2C in Table 4) is the IR component found by Walborn et al. (1999a). Star 1 is P467, while star 3 is P454 and Rubio et al. (1998) IRSW-46, another IR source. The CMDs indicate that there is a coeval cluster with three very red objects in this field, further analysis of which will likely prove rewarding.

The field of P1201 and P1222 in Knot 1 (Fig. 2; the Mount St. Helens pillar) is shown in Figure 11, the photometry is listed in Table 5, and CMDs are shown in Figure 12. Again, both classified components are of late O types. However, the spectrum of P1222 appears peculiar, in that all observed helium lines are of similar intensity; it has been classified as O9 on the basis of He II λ4541 $\approx$ He I λ4387 and He II λ4200 $\approx$ He I λ4144, although He I λ4471 should be relatively much stronger at that type. But the strengths of the weaker He I lines rule out an earlier type. This effect is possibly due to residual nebular emission-line filling at the stronger He I lines. Star 10 is the third-brightest, redder component of the multiple system (Fig. 2). Star 3 is P1164 and star 4 is P1170, classified O3–O6 V in Walborn & Blades (1997); note, however, that P1222 had also been given that type from the ground-based data, similarly to P409, discussed in the previous paragraph. The CMDs again suggest a physical cluster, without any very red objects in this case.

P1429 in Knot 2 (Fig. 3) and its surroundings are charted in Figure 13, photometry is given in Table 6, and the CMDs in Figure 14. In this case, the early O spectral type from Walborn & Blades (1997) is confirmed by the much higher quality STIS data. The spectral type of P1429B (star 4, which includes the even fainter, red third component shown in Walborn et al. 1999a) is very uncertain, since it is derived
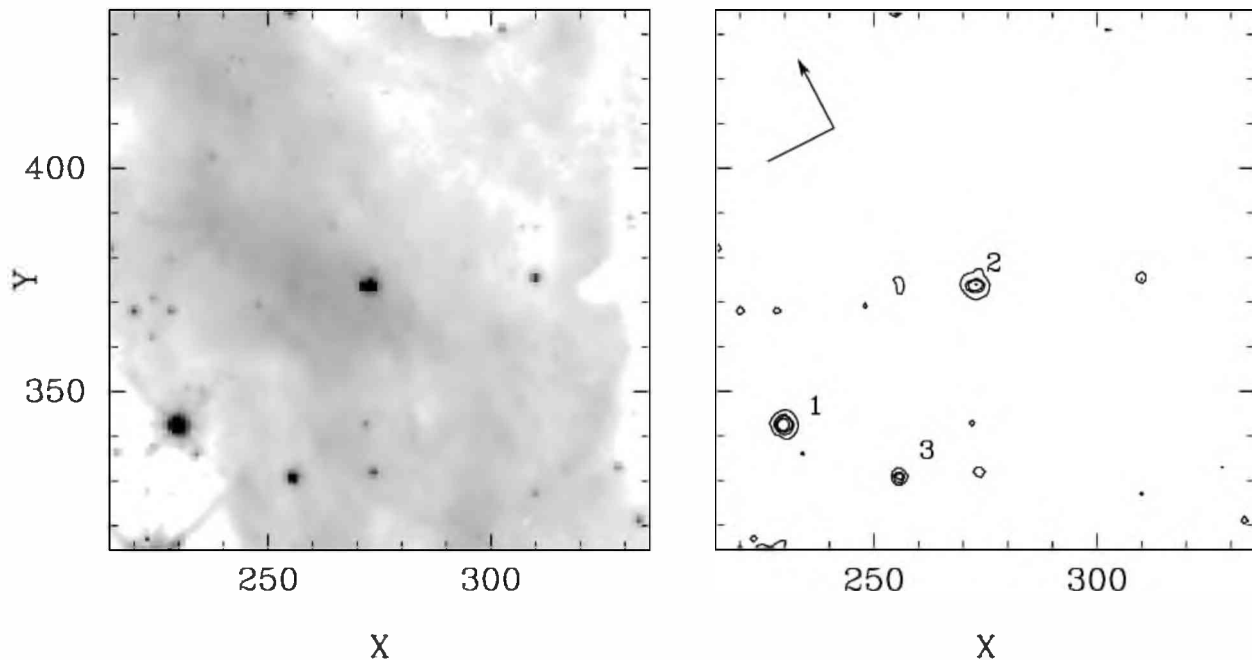

FIG. 9.—Charts of a 12″ square field surrounding P409 in Knot 3; the scales are in WFC pixels (0″.1 pixel^{-1}). An F555W image from *HST* program 5589 is shown at left, and the corresponding contour diagram at right; the compass in the latter indicates north and east . Star 2 is P409; the two nearly equal optical components are barely resolved in the image.

TABLE 4
PHOTOMETRY OF STARS AROUND P409 (KNOT 3)

Star	X^a	Y^a	F555W	σ	F336W−F555W	σ	F555W−F814W	σ
1...........	229.2	342.0	14.66	0.01	−1.18	0.02	0.32	0.01
2A........	273.0	373.2	17.05	0.05	−0.70	0.09	0.47	0.07
2B........	271.4	373.2	17.08	0.05	−0.91	0.08	0.40	0.07
2C........	272.9	376.5	20.64	0.11	...	...	2.07	0.11
3...........	255.1	330.3	17.06	0.01	3.36	0.12	1.82	0.01
4...........	254.4	434.7	18.11	0.01	−1.01	0.03	0.44	0.01
5...........	309.3	374.9	18.82	0.04	−0.81	0.06	0.83	0.05
6...........	273.1	331.4	18.93	0.01	−0.63	0.04	0.46	0.02
7...........	219.6	367.6	19.23	0.01	−0.81	0.03	0.49	0.02
8...........	332.5	320.8	19.43	0.05	−0.58	0.07	0.45	0.06
9...........	309.1	326.8	19.60	0.01	...	...	0.25	0.02
10........	227.7	367.7	19.69	0.01	0.39	0.10	0.20	0.03
11........	301.9	430.7	20.03	0.04	−0.57	0.07	0.52	0.05
12........	271.4	342.2	20.18	0.02	−0.38	0.09	0.33	0.05
13........	223.9	370.4	20.34	0.05	0.04	0.16	0.13	0.09

^{a} Program 5589, chip 4.

from only a low-resolution (G430L), low signal-to-noise ratio observation. The derived M_V would correspond to a normal B2.5 V star on the main sequence (Walborn 1972), which would still have a much higher mass than shown in Table 3. Star 2 is IRSN-138, and star 3 is ISRN-133 (Rubio et al. 1998). The CMDs may correspond to a cluster with many red, embedded objects, but further investigation is required.

4.4.2. First-Generation Systems

The spectroscopic and photometric results for these four systems are listed in the latter part of Table 3. As expected

from their locations, the derived absolute magnitudes and masses are fairly reasonable for the spectral types, consistent with first-generation stars, except for the vignetted stars P1304/P1306, further commented upon below.

P294 and P304 are the brightest members of a small, anonymous cluster at the northern fringe of the extended ionizing association (Fig. 1); it lies beyond the interface but must be in front of the molecular cloud, from the relatively low reddenings (Table 3), the lowest in the present spectroscopic sample. Charts are given in Figure 15, photometry in Table 7, and CMDs in Figure 16. The spectral types are mid and late O, respectively; the relative magnitudes are oppo-
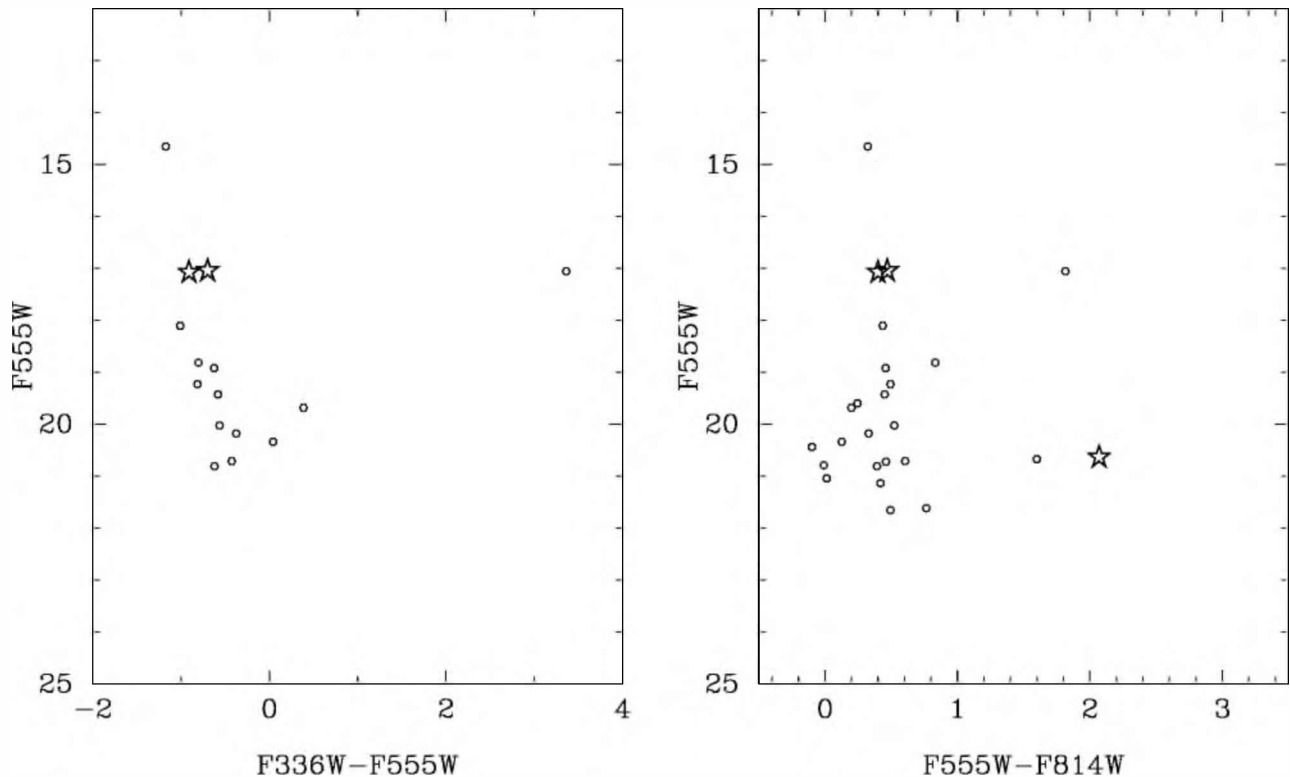

FIG. 10.—Color-magnitude diagrams of the Knot 3 field. The two optical and the IR components of P409 are plotted with five-pointed stars.
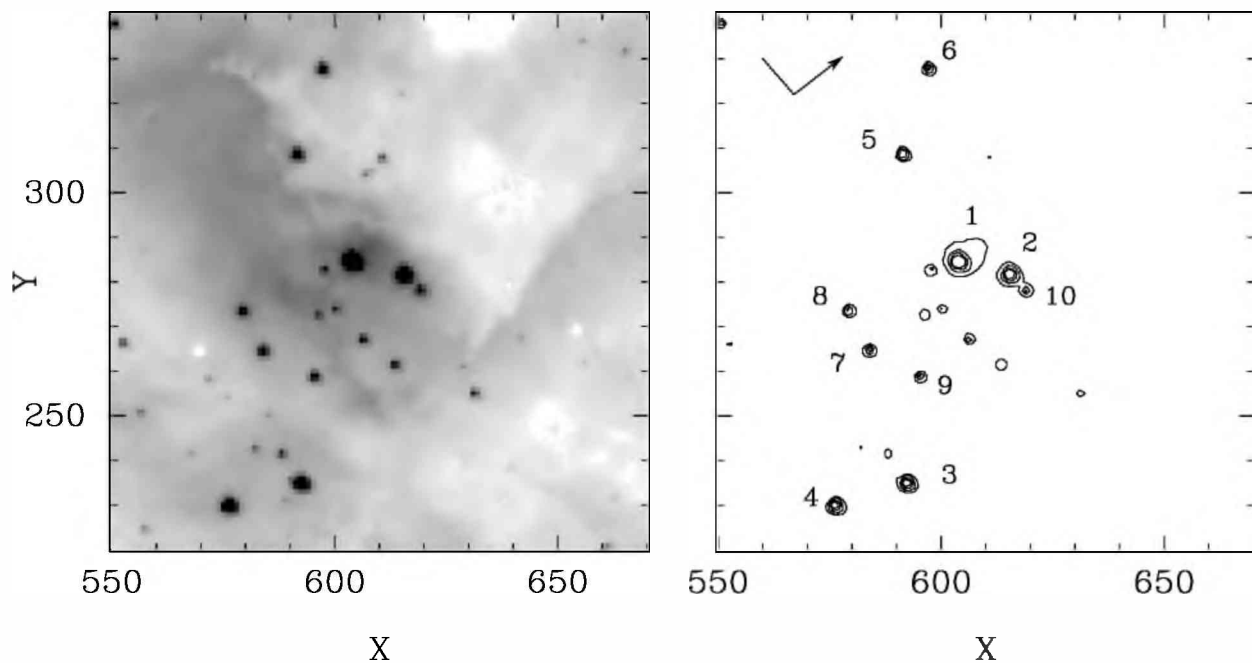
Fig. 11.—Charts of the field of Knot 1 from program 5114, as Fig. 9. Star 1 is P1222 and star 2 is P1201.

TABLE 5
PHOTOMETRY OF STARS AROUND P1201/P1222 (KNOT 1)

| Star	X^a	Y^a	F555W	σ	F336W−F555W	σ	F555W−F814W	σ
1...........	603.3	284.1	15.11	0.01	−1.13	0.01	0.28	0.01
2...........	614.7	281.2	15.83	0.01	−1.28	0.01	0.31	0.01
3...........	591.7	234.4	16.20	0.01	−1.17	0.01	0.27	0.01
4...........	575.7	229.4	16.27	0.01	−1.22	0.02	0.21	0.01
5...........	590.8	308.1	17.06	0.01	−1.11	0.02	0.27	0.01
6...........	596.6	327.3	17.40	0.01	−1.07	0.03	0.43	0.01
7...........	583.3	264.2	17.65	0.01	−1.01	0.03	0.28	0.01
8...........	578.7	273.0	17.82	0.01	−1.19	0.03	0.20	0.01
9...........	594.7	258.3	17.88	0.01	−1.16	0.03	0.27	0.01
10.........	618.5	277.6	18.04	0.01	−0.99	0.04	0.66	0.01
11.........	612.9	260.9	18.43	0.01	−0.91	0.06	0.34	0.01
12.........	605.7	266.6	18.43	0.01	−0.59	0.07	0.55	0.01
13.........	608.1	288.0	18.53	0.01	0.04	0.02	0.12	0.01
14.........	597.1	282.2	18.84	0.01	−1.06	0.06	0.23	0.01
15.........	587.5	240.9	19.00	0.01	−0.83	0.07	0.33	0.01
16.........	595.7	272.1	19.00	0.01	−0.07	0.15	0.26	0.01
17.........	604.8	290.8	19.09	0.01	−0.21	0.03	0.17	0.01
18.........	551.9	265.8	19.19	0.02	−0.70	0.07	0.37	0.03
19.........	599.6	273.4	19.24	0.01	−0.77	0.07	0.30	0.01
20.........	591.0	273.1	19.36	0.05	0.24	0.07	−0.01	0.06
21.........	608.0	273.8	19.37	0.01	−0.36	0.04	0.14	0.01
22.........	609.9	307.1	19.44	0.01	−0.78	0.10	0.24	0.01
23.........	616.4	273.8	19.70	0.01	−0.86	0.04	0.67	0.01
24.........	624.7	266.0	19.77	0.01	0.01	0.04	0.05	0.01
25.........	628.1	260.4	19.82	0.01	−0.16	0.07	0.28	0.01
26.........	581.6	242.1	19.82	0.02	−0.13	0.20	0.44	0.02
27.........	660.6	220.0	20.07	0.02	−0.17	0.25	0.60	0.03
28.........	592.6	268.8	20.12	0.06	0.18	0.07	0.07	0.07
29.........	664.5	331.1	20.14	0.02	−0.27	0.27	0.74	0.03
30.........	555.8	250.1	20.16	0.02	0.06	0.29	0.58	0.02
31.........	606.3	303.6	20.34	0.04	...	...	0.85	0.05
32.........	556.8	224.1	20.46	0.02	...	...	0.41	0.02

^{a} Program 5114, chip 2.
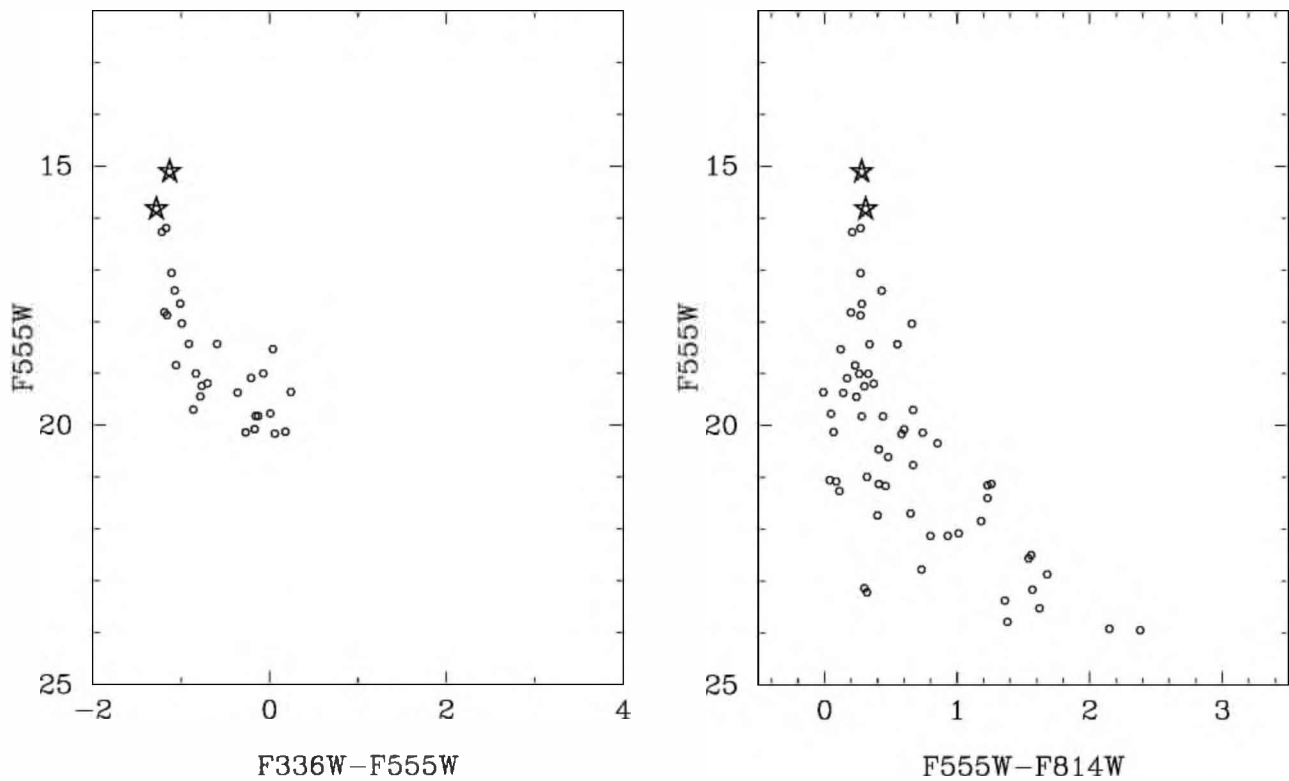
Fig. 12.—CMDs of the Knot 1 field. P1222 and P1201 are plotted with five-pointed stars.

site to what the spectral types predict, suggesting the possibility that P304 may be composite. P304, but likely the combined light of both stars (separation $0\rlap{.}{''}65$; Table 1), was classified O8–O8.5 V in Walborn & Blades (1997), which falls nicely between the spatially resolved types; such agreement is expected when nebular emission-line contamination

is low. Star 4 is P280. The CMDs show a very well defined main sequence, as might be expected for a compact, isolated cluster with little differential extinction.

The multiple systems P1231, P1304/P1306, and P1312 all lie in the same $12''$ square field (Fig. 1), so they are shown together in the charts of Figure 17, but an additional, short-
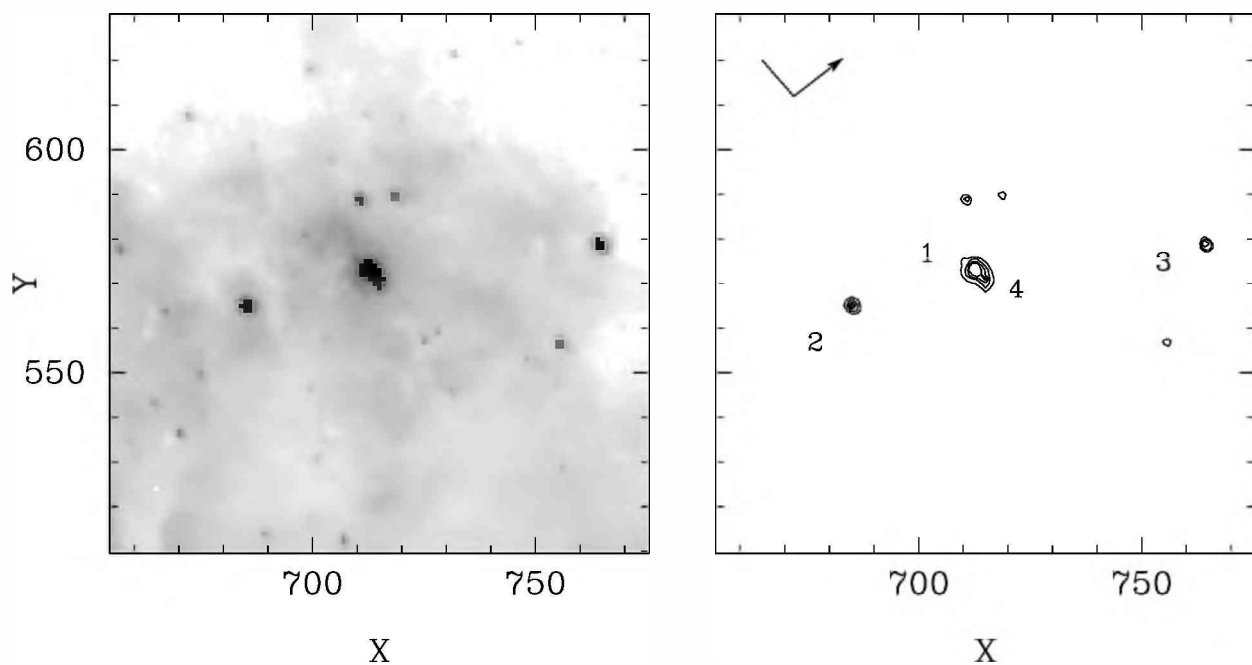

Fig. 13.—Charts of the field of Knot 2 from program 5114, as Fig. 9. Stars 1 and 4 are P1429A and P1429B, respectively.

TABLE 6
PHOTOMETRY OF STARS AROUND P1429 (KNOT 2)

Star	X^a	Y^a	F555W	σ	F336W−F555W	σ	F555W−F814W	σ
1..........	712.0	572.4	15.88	0.02	−1.08	0.05	0.61	0.05
2..........	684.4	564.4	17.78	0.01	...	...	2.13	0.01
3..........	763.8	578.1	17.96	0.01	...	...	1.45	0.01
4..........	714.2	570.1	18.10	0.03	−1.14	0.15	0.54	0.07
5..........	710.1	588.2	19.08	0.01	−0.55	0.06	1.04	0.02
6..........	754.9	556.1	19.64	0.02	...	...	1.39	0.02
7..........	718.1	589.1	19.73	0.01	−0.53	0.08	0.65	0.02
8..........	707.6	580.9	20.14	0.01	−0.78	0.04	0.25	0.02
9..........	698.0	580.7	20.45	0.01	−0.47	0.05	0.24	0.02

^{a} Program 5114, chip 2.

exposure UV image is displayed in Figure 18, to show the very close pairs P1231AB (0″09; Table 1) and P1312AB (0″12) resolved. Photometry for the whole field is listed in Table 8, and the CMDs are shown in Figure 19. The spectral types are in the O5–O8 range; some profiles in the spectrum of P1231A suggest double lines, but further observations would be required to confirm that interpretation. The derived absolute magnitudes of P1304 and P1306 are both 1.1 mag fainter than the calibration values, which is not expected from their spectral types, for example, a giant luminosity class for P1306 (based on the apparent weakening of He II λ4686 absorption relative to the other helium lines; Fig. 8). However, these two stars are in the vignetted region of WFPC2 chip 2, as discussed above, and their derived magnitudes are likely too faint by at least 0.4 mag. Parker (1993) gives substantially brighter magnitudes for

these stars but denotes them as very uncertain in his original thesis, presumably because of mutual blending. Walborn & Blades (1997) classified P1306 (actually the combined light with P1304, separation 0″47) as O8 III, and P1312AB as O7 V, in fair and excellent agreement with the STIS results, respectively. Star 1 is P1253, classified BN0.5 Ia in Walborn & Blades (1997). Stars 4–7 are P1320, P1281, P1248, and P1225, respectively, and there are a number of fainter Parker stars in this field, but none has spectroscopic information to date. The CMDs reveal a perhaps surprisingly tight cluster sequence, given that this is an arbitrary subfield of the ionizing cluster "halo" (Fig. 1). That result is consistent with the stars being a coeval sample of the first stellar generation, although P1253 belongs to an older subpopulation in the field according to the analysis of Walborn & Blades (1997).
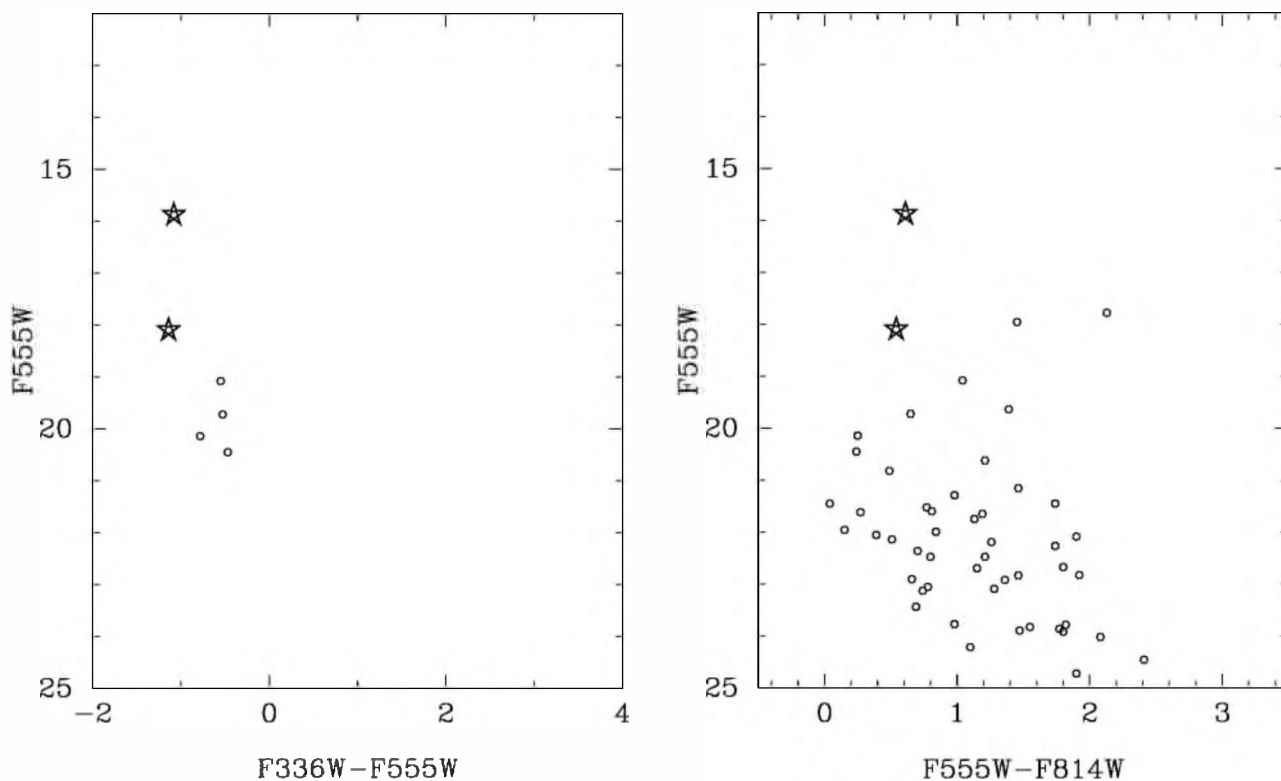

FIG. 14.—CMDs of the Knot 2 field. P1429A and P1429B are plotted with five-pointed stars.
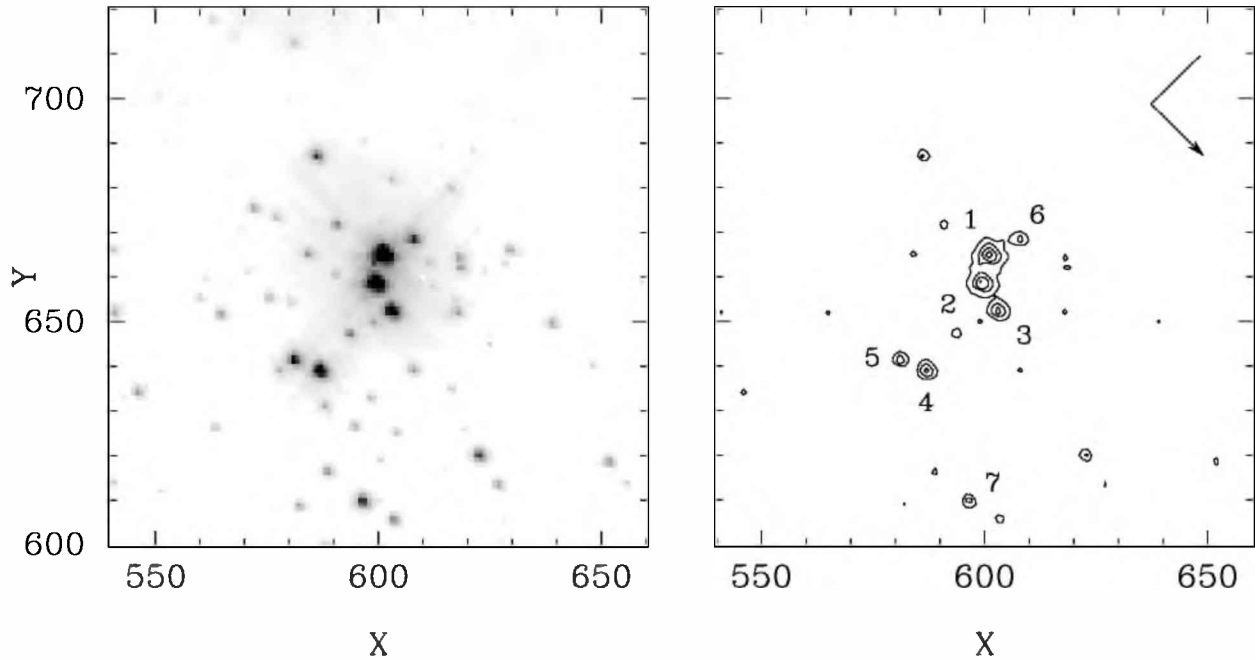
Fig. 15.—Charts of the field of P304/P294 from program 6122, as Fig. 9. Star 1 is P304 and star 2 is P294.

5. SUMMARY AND OUTLOOK

New *HST* observations of 30 Doradus, consisting of WFPC2 images and STIS long-slit optical spectroscopy, have been described. The unifying theme is the intricacy of both nebular and stellar structures in this region, at the spatial resolution of *HST*. A WFPC2 mosaic of the inner nebula reveals its entire structure, including the full extent of the interface between the incipient windblown central cavity and the surrounding molecular clouds, with

TABLE 7
PHOTOMETRY OF STARS AROUND P294/P304

| Star	X^a	Y^a	F555W	σ	F336W−F555W	σ	F555W−F814W	σ
1..........	600.5	664.4	14.47	0.01	−1.51	0.01	0.04	0.01
2..........	599.0	658.0	14.90	0.01	−1.48	0.01	0.13	0.01
3..........	602.5	651.9	16.28	0.01	−1.38	0.01	0.06	0.01
4..........	586.4	638.5	16.51	0.01	−1.21	0.01	0.11	0.01
5..........	580.7	640.9	17.57	0.01	−1.33	0.01	0.08	0.01
6..........	607.3	667.9	17.97	0.01	−1.07	0.03	0.20	0.02
7..........	596.1	609.2	17.99	0.01	−1.21	0.02	0.16	0.01
8..........	622.2	619.5	18.40	0.01	−0.89	0.02	0.19	0.01
9..........	585.8	686.6	18.48	0.01	−1.04	0.02	0.14	0.01
10........	593.2	646.9	19.23	0.01	−0.81	0.03	0.12	0.02
11........	603.0	605.1	19.43	0.01	−0.68	0.03	0.21	0.02
12........	590.4	671.2	19.44	0.01	−0.48	0.05	0.18	0.02
13........	588.2	615.9	19.78	0.01	−0.53	0.04	0.21	0.02
14........	651.2	618.1	19.78	0.01	−0.52	0.04	0.35	0.02
15........	583.8	664.7	19.90	0.01	−0.61	0.07	0.13	0.02
16........	545.6	633.8	19.94	0.01	−0.16	0.06	0.27	0.02
17........	564.3	651.3	20.06	0.01	0.75	0.13	0.49	0.02
18........	618.0	661.7	20.06	0.02	−0.49	0.09	0.28	0.03
19........	617.7	663.9	20.07	0.02	0.04	0.09	0.39	0.03
20........	626.4	613.0	20.10	0.01	−0.18	0.07	0.32	0.02
21........	607.4	638.7	20.13	0.01	−0.32	0.10	0.18	0.03
22........	617.3	651.7	20.16	0.04	−0.18	0.08	0.28	0.08
23........	571.7	675.1	20.26	0.01	−0.23	0.07	0.15	0.03
24........	638.6	649.2	20.29	0.01	−0.41	0.07	0.31	0.03
25........	540.5	651.7	20.29	0.02	−0.13	0.08	0.21	0.05
26........	581.8	608.2	20.31	0.01	−0.21	0.10	0.20	0.02
27........	629.2	665.5	20.33	0.01	0.06	0.09	0.36	0.02
28........	598.3	649.5	20.49	0.08	...	...	0.60	0.09

^{a} Program 6122, chip 2.
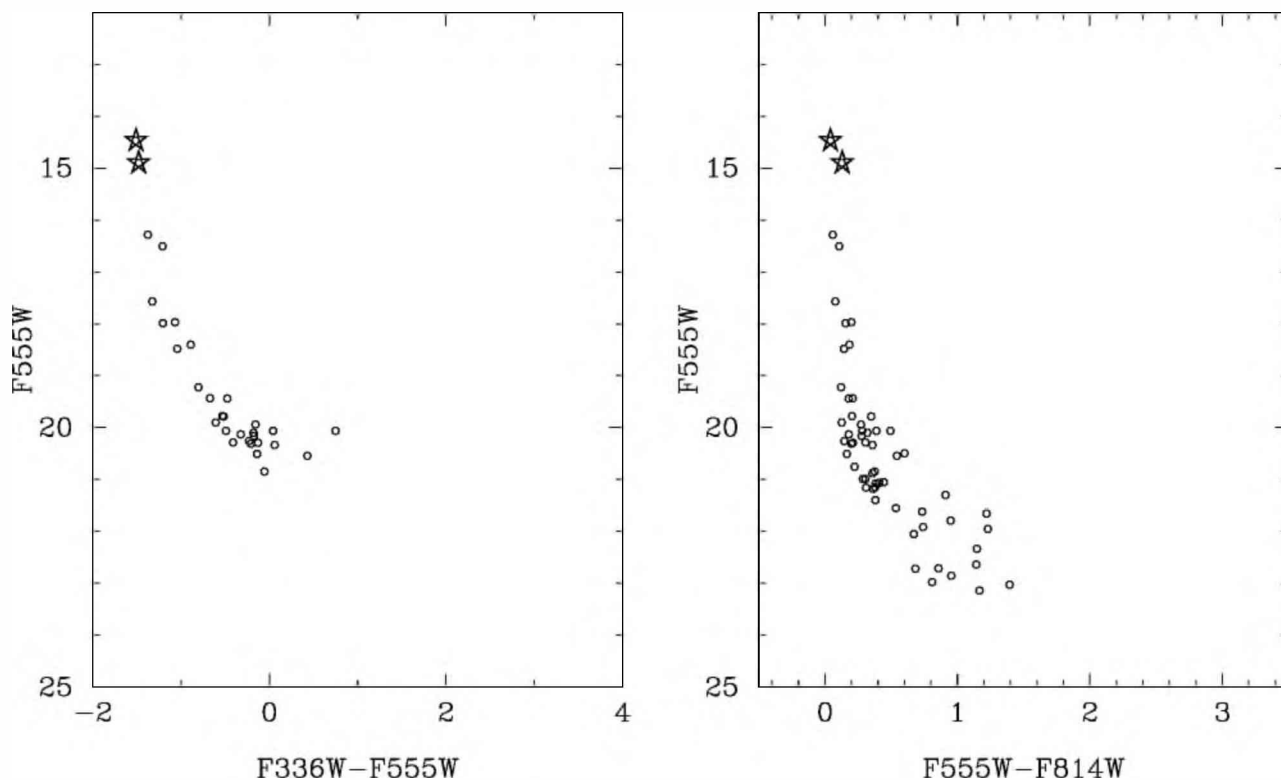
FIG. 16.—CMDs of the P304/P294 field. P304 and P294 are plotted with five-pointed stars.

0″.1 resolution. Particular emphasis has been given to new information about both nebular structures and young stellar multiple systems in the fields of Knots 1–3, representative of the second, triggered generation, obtained from Planetary Camera images with even higher resolution and from STIS spectroscopy, respectively. New WFPC2 coverage of the fields of two luminous IR sources previously observed with NICMOS has been compared with the IR images. Finally, detailed spectroscopic information from STIS about four additional stel-
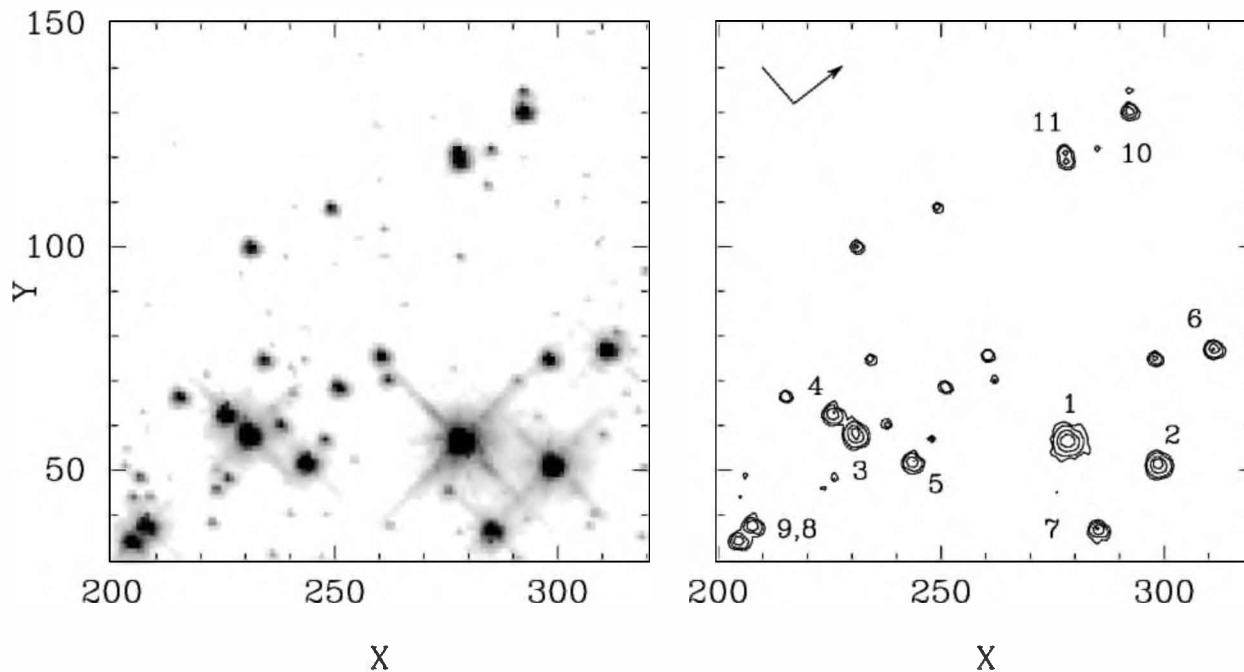

FIG. 17.—Charts of the field of P1231, P1304/P1306, and P1312 from program 5114, as Fig. 9. Star 2 is P1231, star 3 is P1312, and stars 8/9 are P1306/P1304, respectively.
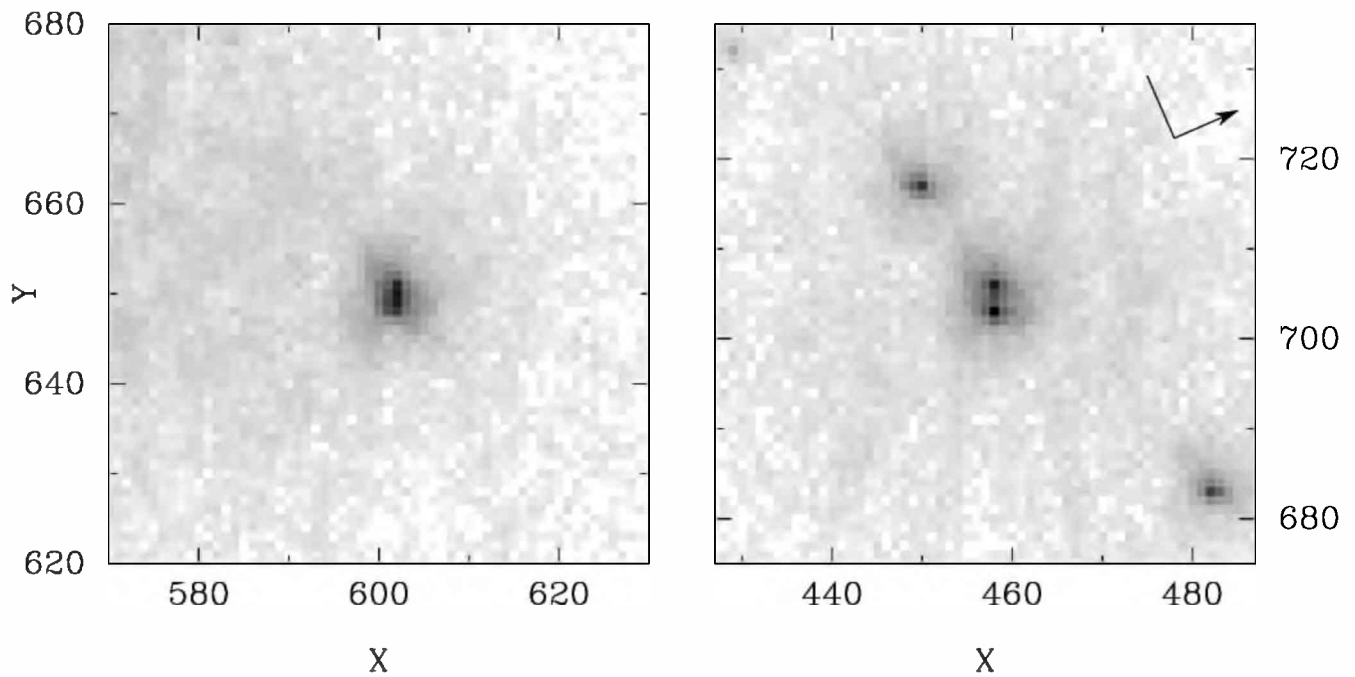
Fig. 18.—Short-exposure (300 s), 3680 Å medium-band continuum images from program 2886, showing the components of P1231AB (*left*) barely and P1312AB (*right*) resolved. This image is from the aberrated PC I (filter F368M); it has not been deconvolved, but the cores of the PSF reveal the multiple systems. Here the pixels are 0″.044 and each panel is 2″.6 square.

lar multiple systems belonging to the first generation has been presented. These data provide valuable insights into both the overall structure of 30 Dor and several sub-regions of special interest, which will be enhanced by planned further analyses that have been mentioned throughout the discussion. Eventually, complete photo-metric studies of both the optical and IR images from *HST* will be combined with available stellar spectroscopic
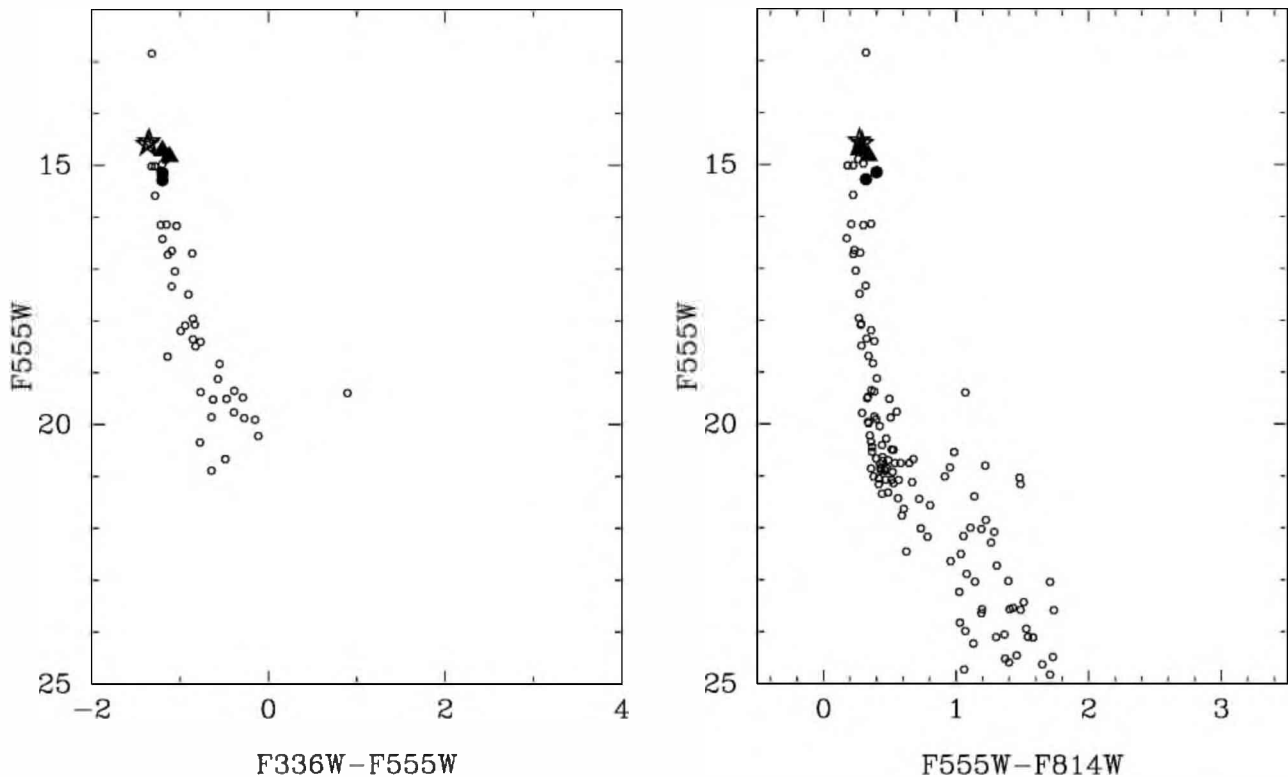

Fig. 19.—CMDs of the P1231, P1304/P1306, P1312 field. *Stars*, P1231AB; *triangles*, P1312AB; *filled circles*, P1304/P1306.

TABLE 8
PHOTOMETRY OF STARS AROUND P1231/P1304/P1306/P1312

Star	X^a	Y^a	F555W	σ	F336W−F555W	σ	F555W−F814W	σ
1..........	277.9	56.1	12.85	0.05	−1.32	0.06	0.32	0.07
2A........	298.1	50.4	14.55	0.03	−1.35	0.04	0.27	0.06
2B........	298.1	51.3	14.61	0.03	−1.37	0.04	0.29	0.06
3A........	230.4	57.1	14.72	0.03	−1.20	0.06	0.27	0.06
3B........	230.1	58.3	14.84	0.03	−1.12	0.06	0.34	0.06
4..........	225.3	62.0	14.90	0.01	−1.17	0.02	0.26	0.01
5..........	243.1	51.3	14.99	0.01	−1.20	0.02	0.30	0.01
6..........	310.6	76.6	15.02	0.01	−1.32	0.01	0.18	0.01
7..........	284.7	36.2	15.03	0.01	−1.29	0.02	0.23	0.01
8..........	207.3	37.2	15.15	0.01	−1.20	0.02	0.40	0.01
9..........	204.1	33.7	15.29	0.01	−1.20	0.02	0.32	0.01
10........	291.8	129.7	15.59	0.01	−1.28	0.01	0.22	0.01
11A......	277.6	118.5	16.15	0.03	−1.15	0.04	0.36	0.04
11B	277.3	120.5	16.17	0.03	−1.04	0.04	0.30	0.04
12........	297.5	74.4	16.19	0.01	−1.22	0.01	0.21	0.01
13........	230.6	99.4	16.42	0.01	−1.20	0.02	0.17	0.01
14........	259.9	75.2	16.66	0.01	−1.09	0.02	0.23	0.01
15........	250.5	68.0	16.70	0.01	−0.86	0.02	0.28	0.01
16........	214.6	65.9	16.73	0.01	−1.14	0.02	0.23	0.01
17........	233.6	74.2	17.05	0.01	−1.06	0.03	0.24	0.01
18........	248.7	108.2	17.34	0.01	−1.09	0.03	0.32	0.01
19........	237.3	59.7	17.49	0.01	−0.90	0.03	0.27	0.01
20........	261.4	69.8	17.96	0.01	−0.86	0.04	0.27	0.01
21........	247.3	56.4	18.07	0.01	−0.83	0.04	0.28	0.01
22........	225.7	47.9	18.09	0.03	−0.94	0.09	0.28	0.05
23........	291.8	134.2	18.20	0.01	−0.99	0.04	0.36	0.01
24........	205.9	48.1	18.36	0.03	−0.86	0.08	0.33	0.04
25........	284.6	121.2	18.41	0.01	−0.77	0.05	0.38	0.01
26........	223.1	45.2	18.50	0.03	−0.83	0.08	0.29	0.04
27........	275.1	44.9	18.69	0.03	−1.14	0.09	0.34	0.04
28........	204.4	43.4	18.83	0.03	−0.55	0.10	0.37	0.04
29........	222.0	37.8	19.12	0.03	−0.57	0.10	0.40	0.04
30........	290.4	69.5	19.35	0.01	−0.39	0.12	0.36	0.01
31........	319.3	94.1	19.38	0.01	−0.77	0.10	0.39	0.01
32........	283.8	113.3	19.39	0.01	0.90	0.29	1.07	0.01
33........	240.1	66.2	19.49	0.01	−0.29	0.15	0.33	0.01
34........	277.6	97.3	19.50	0.01	−0.47	0.12	0.33	0.01
35........	208.1	43.5	19.52	0.05	−0.63	0.13	0.50	0.06
36........	312.8	80.6	19.76	0.03	−0.39	0.23	0.55	0.04
37........	307.9	39.9	19.79	0.02	...	...	0.29	0.03
38........	309.5	57.4	19.86	0.01	−0.64	0.18	0.39	0.01
39........	223.1	49.8	19.88	0.05	−0.28	0.18	0.51	0.07
40........	260.5	103.4	19.91	0.01	−0.15	0.20	0.40	0.01
41........	319.1	50.3	19.97	0.02	...	...	0.34	0.03
42........	202.6	50.6	19.99	0.02	...	...	0.34	0.04
43........	261.9	37.1	20.04	0.02	...	...	0.42	0.03
44........	242.6	74.2	20.22	0.01	−0.11	0.27	0.35	0.01
45........	318.4	34.7	20.28	0.02	...	...	0.47	0.04
46........	306.9	147.3	20.35	0.01	−0.78	0.19	0.36	0.01
47........	239.5	39.8	20.40	0.02	...	...	0.44	0.03
48........	220.6	70.9	20.45	0.02	...	...	0.37	0.03
49........	299.5	109.1	20.49	0.02	...	...	0.52	0.03

[a] Program 5114, chip 2. Stars with $Y < 46$ are vignetted, and their listed magnitudes are too faint.

and nebular molecular data to characterize the complex stellar populations of 30 Doradus, as well as their environment. The *HST* data will endow this enterprise with higher precision than would be feasible from ground-based observations alone.

REFERENCES

Anderson, J., & King, I. R. 1999, PASP, 111, 1095
Barbá, R. H., et al. 2002, in preparation
Biretta, J. A., et al. 2000, Wide Field and Planetary Camera 2 Instrument Handbook (version 5.0; Baltimore: STScI)
Brandner, W., Grebel, E. K., Barbá, R. H., Walborn, N. R., & Moneti, A. 2001, AJ, 122, 858
de Koter, A., Heap, S. R., & Hubeny, I. 1997, ApJ, 477, 792
———. 1998, ApJ, 509, 879
Dolphin, A. E. 2000a, PASP, 112, 1383
———. 2000b, PASP, 112, 1397
Grebel, E. K., & Chu, Y.-H. 2000, AJ, 119, 787
Heydari-Malayeri, M., Royer, P., Rauw, G., & Walborn, N. R. 2000, A&A, 361, 877 (erratum 364, 923)
Holtzman, J. A., et al. 1995, PASP, 107, 156
Hunter, D. A., O'Neil, E. J., Jr., Lynds, R., Shaya, E. J., Groth, E. J., & Holtzman, J. A. 1996, ApJ, 459, L27
Hunter, D. A., Shaya, E. J., Holtzman, J. A., Light, R. M., O'Neil, E. J., Jr., & Lynds, R. 1995a, ApJ, 448, 179
Hunter, D. A., Shaya, E. J., Scowen, P., Hester, J. J., Groth, E. J., Lynds, R., & O'Neil, E. J., Jr. 1995b, ApJ, 444, 758
Hunter, D. A., Vacca, W. D., Massey, P., Lynds, R., & O'Neil, E. J. 1997, AJ, 113, 1691
Hyland, A. R., Straw, S., Jones, T. J., & Gatley, I. 1992, MNRAS, 257, 391
Johansson, L. E. B., et al. 1998, A&A, 331, 857
Koekemoer, A., et al. 2000, HST Dither Handbook (version 1.0; Baltimore: STScI)
Krist, J. 1995, in ASP Conf. Ser. 77, Astronomical Data Analysis Software and Systems IV, ed. R. A. Shaw, H. E. Payne, & J. J. E. Hayes (San Francisco: ASP), 349
Lazendic, J. S., Whiteoak, J. B., Klamer, I., Harbison, P. D., & Kuiper, T. B. H. 2002, MNRAS, 331, 969
MacKenty, J. W., Maíz-Apellániz, J., Pickens, C. E., Norman, C. A., & Walborn, N. R. 2000, AJ, 120, 3007
Massey, P., & Hunter, D. A. 1998, ApJ, 493, 180
Meaburn, J., Solomos, N., Laspias, V., & Goudis, C. 1989, A&A, 225, 497

Parker, J. W. 1993, AJ, 106, 560
Parker, J. W., Clayton, G. C., Winge, C., & Conti, P. S. 1993, ApJ, 409, 770
Parker, J. W., & Garmany, C. D. 1993, AJ, 106, 1471
Parker, J. W., Garmany, C. D., Massey, P., & Walborn, N. R. 1992, AJ, 103, 1205
Parker, J. W., Heap, S. R., & Malumuth, E. M. 1995, ApJ, 448, 705
Rosado, M., Laval, A., Le Coarer, E., Georgelin, Y. P., Amram, P., Marcelin, M., Goldes, G., & Gach, J.-L. 1996, A&A, 308, 588
Rubio, M., Barbá, R. H., Walborn, N. R., Probst, R. G., García, J., & Roth, M. R. 1998, AJ, 116, 1708
Rubio, M., Roth, M., & García, J. 1992, A&A, 261, L29
Scowen, P. A., et al. 1998, AJ, 116, 163
Shaklan, S., Sharman, M. C., & Pravdo, S. H. 1995, Appl. Opt., 34, 6672
Sirianni, M., Nota, A., Leitherer, C., De Marchi, G., & Clampin, M. 2000, ApJ, 533, 203
Stetson, P. B. 1987, PASP, 99, 191
Vacca, W. D., Garmany, C. D., & Shull, J. M. 1996, ApJ, 460, 914
Walborn, N. R. 1972, AJ, 77, 312
———. 1973, AJ, 78, 1067
———. 1991, in Massive Stars in Starbursts, ed. C. Leitherer, N. R. Walborn, T. M. Heckman, & C. A. Norman (Cambridge: Cambridge Univ. Press), 145
———. 2002, in ASP Conf. Ser. 267, Hot Star Workshop III: The Earliest Stages of Massive Star Birth, ed. P. A. Crowther (San Francisco: ASP), 111
Walborn, N. R., Barbá, R. H., Brandner, W., Rubio, M., Grebel, E. K., & Probst, R. G. 1999a, AJ, 117, 225
Walborn, N. R., & Blades, J. C. 1987, ApJ, 323, L65
———. 1997, ApJS, 112, 457
Walborn, N. R., Drissen, L., Parker, J. W., Saha, A., MacKenty, J. W., & White, R. L. 1999b, AJ, 118, 1684
Walborn, N. R., et al. 2002, AJ, 123, 2754
Walborn, N. R., & Parker, J. W. 1992, ApJ, 399, L87
Werner, M. W., Becklin, E. E., Gatley, I., Ellis, M. J., Hyland, A. R., Robinson, G., & Thomas, J. A. 1978, MNRAS, 184, 365